STEADY AND UNSTEADY AERODYNAMIC ANALYSIS OF THE AIRFOIL PROFILES BY USING VORTEX SINGULARITY ELEMENTS

A Thesis Submitted to
the Graduate School of Engineering and Sciences of
İzmir Institute of Technology
in Partial Fulfillment of the Requirements for the Degree of

MASTER OF SCIENCE

in Energy Engineering

by
Salim Cenk ELMACI

July 2018
İZMİR

We approve the thesis of **Salim Cenk ELMACI**

Examining Committee Members:

Assoc. Prof. Dr. Ünver ÖZKOL
Department of Mechanical Engineering, İzmir Institute of Technology

Assoc. Prof. Dr. Erdal ÇETKİN
Department of Mechanical Engineering, İzmir Institute of Technology

Dr. Ziya Haktan KARADENİZ
Department of Mechanical Engineering, İzmir Katip Çelebi University

10/July/2018

Assoc. Prof. Dr. Ünver ÖZKOL
Supervisor, Department of Mechanical Engineering
İzmir Institute of Technology

Dr. Bergüzar ÖZBAHÇECİ
Co-Supervisor, Department of Civil Engineering
İzmir Institute of Technology

Prof. Dr. Gülden GÖKÇEN AKKURT
Head of the Department of Energy Engineering

Prof. Dr. Aysun SOFUOĞLU
Dean of the Graduate School of Engineering and Sciences

ACKNOWLEDGEMENTS

First and foremost, I would like to thank to my advisors Assoc. Prof. Dr. Ünver ÖZKOL and Asst. Prof. Dr. Bergüzar ÖZBAHÇECİ for their precious advice and motivation on my thesis. It was a pleasure for me to conduct my research under their supervising.

I gratefully thank to my colleague Çağatay KÖK for his support in the key points of the CFD simulation. Furthermore, I would like to thank Cevahir KARAGÖZ and Önder Mahir TANRIYAPISI for their helpful leading in the programming issues. Moreover, I owe a debt of gratitude to my roommates Can SINDIRAÇ and Doğuş ZEREN; my neighbors Altuğ ÇAVUŞOĞLU and Emre Yusuf GÖL; my friends Ege TUNCER and Nezih Gökhan ÖZÇELİK for their friendship and encouragement for last two years.

I am thankful to my family: my relatives Behiye Serap ELMACI, Ayşe Semra ELMACI and Burak KUMPASOĞLU who have had extremely important contributions on my personal and intellectual development; my mom Suphiye ELMACI and my brother Rasim Mennan ELMACI.

Lastly, I would like to thank to a very special person, Gizem Saraçer, for her moral support during my thesis study. I would like to thank to everyone who helped me during this study.

ABSTRACT

STEADY AND UNSTEADY AERODYNAMIC ANALYSIS OF THE AIRFOIL PROFILES BY USING VORTEX SINGULARITY ELEMENTS

The steady and unsteady 2D flows around the airfoil were analyzed by utilizing the vortex singularity elements with two different inviscid flow models. Firstly, the steady flow was modeled in the light of steady state algorithm available in the literature. Then, the unsteady flow model was developed by some modifications on the algorithm of the steady flow. All the algorithms were transformed to the code in MATLAB® 2018a environment. For the steady state model, lift coefficients were compared with the inviscid and inviscid-viscous coupling models of the Xfoil 6.9 program data (Drela, 2001); and NASA experimental archive (Ira Herbert Abbott & Von Doenhoff, 1959). Since the model is inviscid, the reference point is the inviscid solvers; and the model agreed well with the Xfoil 6.9 inviscid mode for different type of airfoils. The unsteady model was created with three different operating modes; which are the sudden forward, heaving and the pitching. For the sudden forward motion, the lift and drag coefficients were compared with the studies in the literature. Besides, the lift, drag moment coefficients; and the wake patterns of the heaving and pitching motions were compared with the experimental data in the literature. The model is limited in terms of reflecting lift, drag and moment coefficients due to the not being included the viscous effects, flow separation, stall etc.; however, in terms of capturing the wake patterns, the model is quite useful.

ÖZET

KANAT PROFİLLERİNİN VORTEKS TEKİLLİK ELEMANLARI KULLANILARAK SÜREKLİ VE SÜREKSİZ AERODİNAMİK ANALİZİ

2 boyutlu kanat profili etrafındaki sürekli ve süreksiz akışlar, vorteks tekillik elemanları kullanılarak oluşturulan iki farklı ideal akış temelli bir model ile analiz edilmiştir. İlk olarak, sürekli akış, literatürde bulunan algoritmalar ışığında modellenmiştir. Daha sonra, sürekli akış modelinin algoritmasında küçük değişiklikler yapılarak süreksiz akış modeli geliştirilmiştir. Bütün algoritmalar, MATLAB® 2018a ortamında koda dökülmüştür. Sürekli akış modeli için, kaldırma kuvveti katsayısı Xfoil 6.9 programının ideal, ideal-viskoz birleşik modelleri (Drela, 2001) ve NASA deneysel arşivindeki veriler (Ira Herbert Abbott & Von Doenhoff, 1959) ile karşılaştırılmıştır. Model, ideal akış yaklaşımıyla modellendiğinden, kıyaslama için aynı yaklaşıma sahip modeller temel alınmıştır ve model Xfoil 6.9 viskoz olmayan çözümü ile oldukça yakın sonuçlara sahiptir. Süreksiz akış modeli, ani sabit hızla ileriye doğru, dalıp-çıkma ve yunuslama olmak üzere üç farklı hareketi çalıştırma özelliğine sahip olacak şekilde geliştirilmiştir. Ani sabit hızla ileriye doğru harekete ilişkin kaldırma kuvveti ve sürükleme kuvveti katsayıları literatürdeki çalışmalar ile karşılaştırılmıştır. Bunun yanında, dalıp-çıkma ve yunuslama hareketlerine ilişkin basınç, kaldırma kuvveti, sürükleme kuvveti ve moment katsayıları deneysel literatür ile karşılaştırılmıştır. Viskoz etkiler, akış ayrılması vs. dikkate alınmadığından, model, kaldırma kuvveti, sürükleme kuvveti ve moment katsayılarını yansıtmak açısından sınırlıdır; ancak, art akış izlerini yakalamakta oldukça başarılı olduğu gözlemlenmiştir.

TABLE OF CONTENTS

LIST OF FIGURES

Figure **Page**

CHAPTER 1

INTRODUCTION

Numerical Panel Methods are the solution methods in fluid mechanics which use singularity elements in potential flow theory to model the flow field by numerical discretization of flow domain. They are commonly preferred due to their faster analysis ability compared to the Navier-Stokes equations based CFD models in terms of computation time (Joseph Katz & Plotkin, 2001). However, even if the application of these techniques is efficient for calculation of lift force and lift coefficient of the airfoil; or modelling the flow field around the lowly cambered geometries etc., detailed analysis of the complex flow fields such as turbulent flows etc. through panel methods cannot be considered as useful. Nevertheless, hybrid models such as viscous-inviscid interaction models, panel methods with stall models etc. are developed to create both relatively time efficient and enough detailed solution techniques (Zanon, Giannattasio, & Simão Ferreira, 2013)

The panel methods are fundamentally classified according to type of singularity element. After selection of singularity element, the boundary condition is applied. While singularity elements source, vortex, doublet may be chosen separately, the combination of these may also be chosen to create a panel method for modelling. One of these element, the vortex element is useful especially for modelling lifting problems of the airfoils because of the ability to represent the effect of the cambering in the airfoil (Anderson, 2016).

In the present study, the vortex singularity element was chosen to generate a panel method to model the flow field around the airfoil for steady and unsteady flow cases. In this context, firstly, steady state panel model was developed, and then, the unsteady panel model was developed by the several modifications on the algorithm that used in the steady state model. Unsteady model was specifically created an attempt to constitute a basic knowledge for the fundamentals of the aerodynamics of floating wind turbine problems. All the program codes were written, and the figures were plotted in the MATLAB® 2018a environment. After those, for the steady part, the results were compared with the Xfoil

6.9 inviscid and inviscid-viscous coupling models; and NASA experimental archive. The results by the unsteady part were compared with numerical and the experimental literature.

The content of the thesis is as follows: In Chapter II, the vortex panel method for steady state flow is treated. Unsteady flow model is given in Chapter III. Chapter IV contains the result and discussion. Conclusion are made in Chapter V.

In the sections 1.1-1.4, the introductory knowledge was given by referring to the details expressed in the textbook "Low-Speed Aerodynamics" (Joseph Katz & Plotkin, 2001).

1.1. Introduction to Numerical Panel Methods

There are various approaches to solve the potential flow problems. One of them is, the analytical techniques that are preferred due to being exact and computationally time efficient. However, to implement a such kind of technique, major simplifications in the problem geometry where boundary conditions were applied must be done; this situation limits the ability of these techniques.

The other approach is the numerical panel methods where the advantage lies in the flexibility to deal with more realistic geometries. Moreover, boundary conditions can be directly applied on to the actual problem surface.

The numerical methods use the philosophy originated from the analytical techniques, that is to implement the singularity elements on the actual surface of the geometry and to find their strengths. This technique allows us to reduce the computational time compared to the finite difference methods for potential flows.

1.2. Mathematical Fundamentals of the Numerical Solution Technique

Assume a flow field **V** which is defined as the outer region of the body S_B, a body such that its boundaries are determined, and this flow field is potential, Fig. 1. If the incompressible continuity equation is written for a potential flow one would obtain a Laplace equation for total potential Φ^* which is expressed in the frame of reference attached to the body:

$$\nabla^2 \Phi^* = 0 \tag{1.1}$$

Since the Green's Identities is preferred to generate a solution for the Laplace equation; in this context, the general solution which is composed of the combination of source σ and μ doublet elements can be offered:

$$\Phi^*(x,y,z) = -\frac{1}{4\pi}\int_{S_B}\left[\sigma\left(\frac{1}{r}\right) - \mu \mathbf{n}\bullet\nabla\left(\frac{1}{r}\right)\right] dS + \Phi_\infty \tag{1.2}$$

Where, the Φ_∞ is the freestream potential. The vector n shows the direction the potential jump μ; it is aligned normal to the body S_B and positive outside of **V**. (Fig. 1)

$$\Phi_\infty = U_\infty x + V_\infty y + W_\infty z \tag{1.3}$$

This equation is a "general" solution not a unique one for the given boundary conditions, since, it may be written in many different distributions of source and doublet singularity elements.

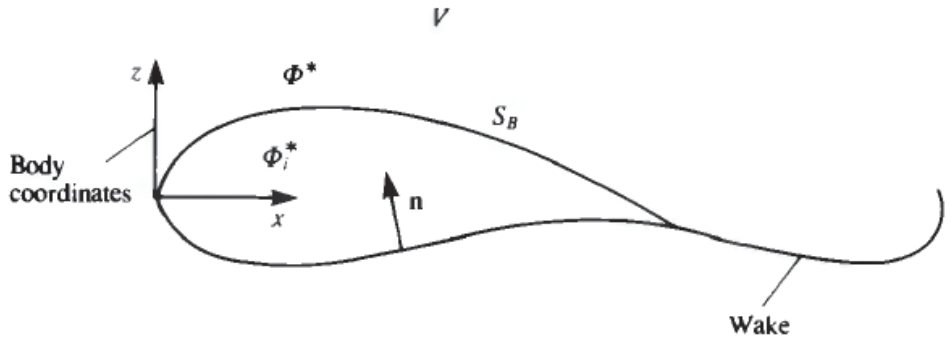

Figure 1. Arbitrary body in the flow field (Source: Joseph Katz and Plotkin (2001))

Keep in mind that, the source elements are used to reflect the effect of thickness, the vortex and doublet elements are preferred to model lifting effect on the closed bodies in the potential flow field. To find a unique solution for the potential flow problem in here, there are two necessities; boundary conditions and the physical considerations.

Problem setup procedure can be summarized as; first is to start with arbitrary choice of combination of singularity elements. Then, the necessary physical considerations which are regarding the modelling of the wakes and their features must

have a role to find the amount of circulation. This is a critical step in the problem solution in which without them, the boundary conditions are not able to generate a unique solution. Moreover, it should be noted that, the wake part can be modeled by the thin vortex or doublet sheets; thus, it is sensible to rearrange the Eq. 1.1 in terms of ease of understandability as:

$$\Phi^*(x,y,z) = \frac{1}{4\pi}\int_{Body+Wake}\left[\mu \mathbf{n}\bullet\nabla\left(\frac{1}{r}\right)\right]dS - \frac{1}{4\pi}\int_{Body}\sigma\left(\frac{1}{r}\right)dS + \Phi_\infty \tag{1.4}$$

The basic two boundary conditions for Eq. 1.1 can be expressed as; the first one is the Neumann type of boundary condition; which is also defined as zero normal flow on the body surface $\frac{\partial \Phi*}{\partial n} = 0$. The second one is the Dirichlet type of boundary condition; the boundary condition that specify a constant value for the potential inside (without internal singularities) the body $\Phi^* \equiv constant$. The Neumann and Dirichlet problems are called as "direct" and "indirect" formulations respectively. Furthermore, the combination of the both boundary conditions can be applied together which is also known as mixed boundary condition.

Another formulation which approaches to the problem from the view of the streamline functions may also be used; yet, it is meaningful to use that approach for 2D problems, not for the complex, 3D geometries owing to the difficulty of application.

Although the general solution perspective of the panel methods is given in this Chapter, this study aims to model the flow around an airfoil only by vortex elements and the application of the Neumann boundary condition is our main concern. In this direction, let's start with the expression of that:

$$\nabla\Phi^*\bullet\mathbf{n} = 0 \tag{2.5}$$

or in an open form:

$$\nabla(\Phi + \Phi_\infty)\bullet\mathbf{n} = 0 \tag{2.6}$$

Where Φ and Φ_∞ are the perturbation and freestream potentials respectively. Besides, substitution of the Eq. 1.4 into the Eq. 1.6 is given as:

$$\left\{\frac{1}{4\pi}\int_{Body+Wake}\mu\nabla\left[\frac{\partial}{\partial n}\left(\frac{1}{r}\right)\right]dS-\frac{1}{4\pi}\int_{Body}\sigma\nabla\left(\frac{1}{r}\right)dS+\nabla\Phi_{\infty}\right\}\bullet\mathbf{n}=0 \qquad (2.7)$$

For many type of panel problems, the Eq. 1.7 is the fundamental starting point. Since this equation is applied on each collocation points (the point where the boundary condition is applied) which are on the surface S_B, and the integral equation will be transformed to a set of algebraic equations.

Further details of the problem setup about the wake region will be given in the Chapter 2. Though, for now, to demystify the main philosophy, it is significant to express the physical conditions which are the necessity to generate unique solution for the flow problem in terms of the "wake model". Accordingly, there are two issues regarding to the wake model:

- The strength of wake at the trailing edge
- The location and shape of the wake

1.3. Preliminary Concepts

Before starting to solution of the panel problem, these concepts should be considered.

- Type of singularity element
- Boundary Condition
- Wake Model
- Discretization of Geometry and Singularity Element Distribution
- Numerical Efficiency

1.4. Steps of Numerical Solution

The problem solution steps can be expressed as (similarly is shown in Fig. 2):

- Choice of Singularity Element
- Meshing Geometry
- Computation of Influence Coefficients
- Establishing Right Hand Side Vector

- Solution of Linear Set of Equations
- Calculation of Velocity, Pressure, Loads, etc.

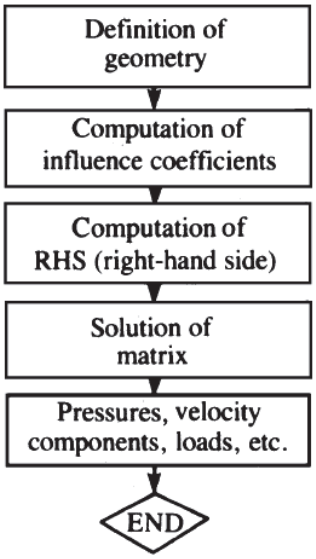

Figure 2. Steps of numerical solution proposed in the “Low-Speed Aerodynamics” (Source: Joseph Katz and Plotkin (2001))

CHAPTER 2

STEADY PANEL METHOD

2.1. Introduction

The thin airfoil theory satisfies the demand of the aerodynamic lift analysis of an airfoil which has a small thickness (12% or less) and small camber at small angles of attacks. However, if the airfoil thickness and angle of attack are larger or the problem geometry is different such as automobiles, submarines etc., another approach, a generalized method that can handle these issues is needed. In this context, since the early 1970s, scientists started to use the method called as vortex panel method. The method is analogous to the source panel method in terms of many ways, nevertheless, with a difference that source panel is applicable for only non-lifting cases while the vortex panel can be used for lifting cases. The idea of vortex panel method is to implement a vortex sheet on the body surface such that the surface becomes the streamline of the flow and Kutta Condition is satisfied. (Explained in the section 2.2.3.) The singularity element that is used in each panel on vortex sheet can be either constant strength or linearly varying strength; which makes the method either the first order or second order respectively. The solution of the first order panel methods gives rise to "overdetermined" set of equations. Besides, compared to the second order (linear) methods, they are less efficient in terms of reflecting the vortex strength distribution. Since, second order (linear) panel methods are preferred in the modelling (Anderson, 2016).

2.2. Steady Panel Method

The second order (linear) steady state panel code was developed in the MATLAB® 2018a environment for the Chapter 2 according to the textbook "Foundations of Aerodynamics: Bases of Aerodynamic Design" (Kuethe & Chow, 1997). Furthermore, to make the steps clearer, some of the equations and figures which had been given in "The Vortex Panel Method" (Tavoularis, n.d.) were used.

2.2.2. Choice of Singularity Element

Since the second order method is preferred, each vortex panel has linear strength distribution in which end vortex strength of any panel is equal to the starting vortex strength of the panel next to it. (Shown in Fig. 3)

$$\gamma(s_j) = \gamma_j + \frac{s_j}{S_j}(\gamma_{j+1} - \gamma_j) \tag{2.1}$$

Where j is the number of a panel, and $j = 1, 2, ..., m+1$. Excluding: $\gamma_1 \neq \gamma_{m+1}$

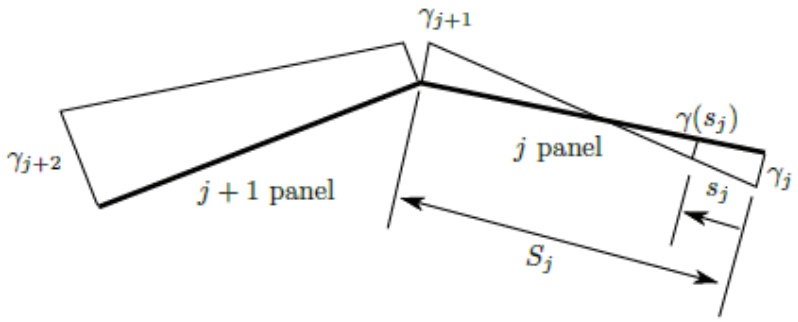

Figure 3. Linear variation of vortex strength along the panels (Source: Tavoularis (n.d.))

2.2.3. Meshing Geometry

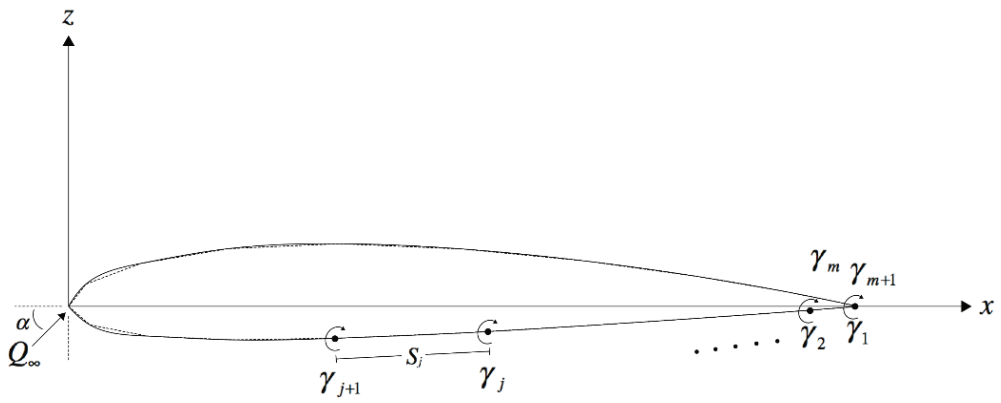

Figure 4. Discretized airfoil geometry

Discretize the airfoil geometry to inscribe a polygon with m sides. Here the sides are represented by the flat *panels*. panels are numbered by starting from the trailing edge of the airfoil and proceeding in clockwise direction such that panels #1 and #m are to

become lower side and upper side at the trailing edge, respectively. This process is represented in Fig. 4.

At this stage, the airfoil coordinate data is discretized such that the higher the radius of curvature, the larger the mesh size; in this way, a useful data which gives the higher sensitivity around where the radius of curvature is lower on the airfoil geometry can be obtained.

2.2.4. Computation of Influence Coefficients

The unknowns of the problem are the vortex strengths γ_j, $j=1,2,...,m+1$. To find their values, m+1 equations are needed. m+1 equations are established as follows:

a. m number of equations: equations can be established by writing zero normal flow condition (Neumann B.C.) for the midpoint of each panel (a.k.a. the control point) Remember that the gradient of the potential equals to the velocity vector:

$$\nabla\Phi = \mathbf{V} \tag{2.2}$$

Then, total velocity component in panel normal vector, $\mathbf{n}_i$ is (orientation of the normal vector is given in Fig. 5):

$$Q_{ni} = \frac{\partial\Phi^*}{\partial\mathbf{n}_i} \tag{2.3}$$

Consequently, Neumann boundary condition is written for all panels:

$$\frac{\partial\Phi^*(x_i, z_i)}{\partial\mathbf{n_i}} = 0, \ where\ i = 1, 2, \ \dots\ , \ m \tag{2.4}$$

b. Kutta Condition at the trailing edge gives one more equation that is needed to satisfy the physical reality of the flow. One way of writing Kutta condition is by the summation of upper and lower velocity terms at the trailing edge which must be zero; in other words, the vortex strength at the trailing edge is zero:

$$\gamma_1 + \gamma_{m+1} = 0 \tag{2.5}$$

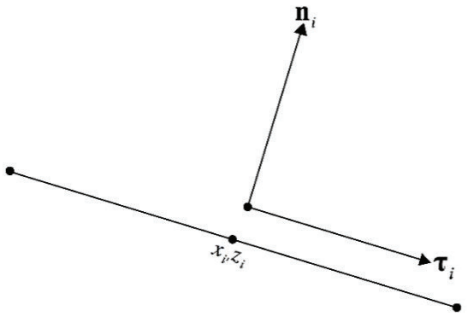

Figure 5. Normal and tangential vectors on the i^{th} panel

After the solution of the m+1 equations and then computation of the γ_j values, the velocity is obtained by superposition of potentials. Afterwards pressure is calculated through the Bernoulli's equation.

The perturbation potential induced at the i^{th} control point due to the panel j is:

$$\Delta\Phi_j = -\frac{1}{2\pi}\int_j \gamma(s_j)\tan^{-1}\frac{z_i - z_j}{x_i - x_j}ds_j \tag{2.6}$$

Therefore, the perturbation potential induced at the i^{th} control point due to the m panels is:

$$\Phi_j(x_i, z_i) = \sum_{j=1}^{m}\int_j \frac{-\gamma(s_j)}{2\pi}\tan^{-1}\frac{z_i - z_j}{x_i - x_j}ds_j \tag{2.7}$$

Moreover, the freestream potential at the i^{th} control point due to free stream is:

$$\Phi_\infty(x_i, z_i) = Q_\infty(x_i\cos\alpha + z_i\sin\alpha) \tag{2.8}$$

Finally, the total velocity potential at the i^{th} control point is the summation of the potential due to the free stream and potential induced due to the m panels:

$$\Phi^*(x_i, z_i) = Q_\infty (x_i \cos\alpha + z_i \sin\alpha) - \sum_{j=1}^{m} \int_j \frac{\gamma(s_j)}{2\pi} \tan^{-1} \frac{z_i - z_j}{x_i - x_j} ds_j \qquad (2.9)$$

The angular relation between the panels i and j is given in the Fig. 6.

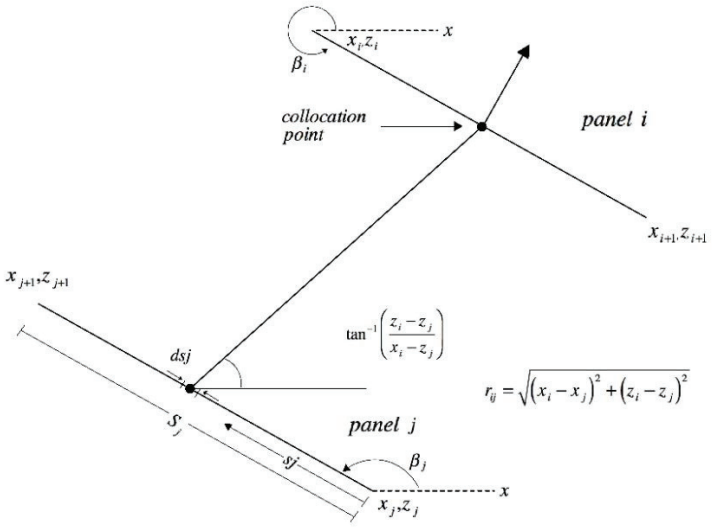

Figure 6. Angular relation between the i^{th} and j^{th} panels

The application of Neumann boundary condition can be written in an open form by using the chain rule in differentiation:

$$\frac{\partial \Phi}{\partial \mathbf{n_i}} = \frac{\partial \Phi}{\partial x_i} \frac{\partial x_i}{\partial \mathbf{n_i}} + \frac{\partial \Phi}{\partial z_i} \frac{\partial z_i}{\partial \mathbf{n_i}} \qquad (2.10)$$

Remember that:

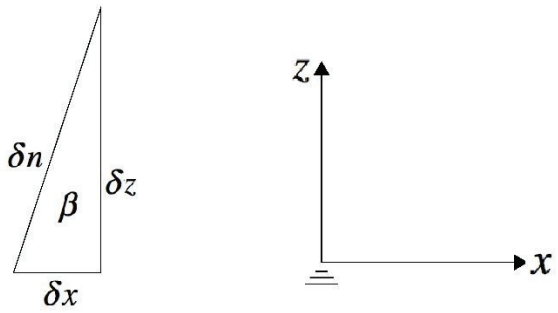

Figure 7. Relation among the δx, δz and δn

In the light of geometric relationship represented in the Fig. 7:

$$\frac{\partial x_i}{\partial \mathbf{n_i}} \approx \frac{\delta x_i}{\delta \mathbf{n_i}} = \sin \beta_i \tag{2.11}$$

$$\frac{\partial z_i}{\partial \mathbf{n_i}} \approx \frac{\delta z_i}{\delta \mathbf{n_i}} = \cos \beta_i \tag{2.12}$$

Thus, the equation 3.10 becomes:

$$\frac{\partial \Phi}{\partial \mathbf{n_i}} = \frac{\partial \Phi}{\partial x_i} \sin \beta_i + \frac{\partial \Phi}{\partial z_i} \cos \beta_i \tag{2.13}$$

If the integral in the equation 3.9. is differentiated, the following terms will be obtained:

$$\frac{\partial}{\partial x_i}\left[\tan^{-1}\frac{z_i - z_j}{x_i - x_j}\right] = \frac{-1}{1+\left(\frac{z_i - z_j}{x_i - x_j}\right)^2}\frac{z_i - z_j}{(x_i - x_j)^2} \tag{2.14}$$

$$\frac{\partial}{\partial z_i}\left[\tan^{-1}\frac{z_i - z_j}{x_i - x_j}\right] = \frac{1}{1+\left(\frac{z_i - z_j}{x_i - x_j}\right)^2}\frac{1}{x_i - x_j} \tag{2.15}$$

To evaluate the integral, let's rewrite the x_j and z_j in terms of s_j:

$$x_j = X_j - s_j \cos \beta_j \tag{2.16}$$

$$z_j = Z_j + s_j \sin \beta_j \tag{2.17}$$

Furthermore, $\gamma(s_j)$ must be written in terms of s_j. Hence, the integral in Eq. 2.9 turns out the summation of the two integral parts:

$$\gamma_j \int_0^{S_j} f_{1j}(s_j) ds_j + \gamma_{j+1} \int_0^{S_j} f_{2j}(s_j) ds_j \tag{2.18}$$

If these two integrals are evaluated for all the panels, the following linear equation reveals:

$$\sum_{j=1}^{m}\left(Cn1_{ij}\gamma_j + Cn2_{ij}\gamma_{j+1}\right) = Q_\infty \sin(\beta_i - \alpha) \quad where\ i = 1,2,...,m \tag{2.19}$$

$Cn1_{ij}$ and $Cn2_{ij}$ coefficients are:

$$\begin{aligned} Cn1_{ij} &= \frac{1}{2\pi}\left(0.5DF + CG\right) - Cn2_{ij} \\ Cn2_{ij} &= \frac{1}{2\pi}\left(D + 0.5QF / S_j - (AC + DE)G / S_j\right) \end{aligned} \tag{2.20}$$

Where;

$$\begin{aligned} A &= -(x_i - X_j)\cos\beta_j - (z_i - Z_j)\sin\beta_j \\ B &= (x_i - X_j)^2 + (z_i - Z_j)^2 \\ C &= \sin(\beta_i - \beta_j) \\ D &= \cos(\beta_i - \beta_j) \\ E &= (x_i - X_j)\sin\beta_j - (z_i - Z_j)\cos\beta_j \\ F &= \ln\left(1 + \frac{{S_j}^2 + 2AS_j}{B}\right) \\ G &= \tan^{-1}\left(\frac{ES_j}{B + AS_j}\right) \\ P &= (x_i - X_j)\sin(\beta_i - 2\beta_j) + (z_i - Z_j)\cos(\beta_i - 2\beta_j) \\ Q &= (x_i - X_j)\cos(\beta_i - 2\beta_j) - (z_i - Z_j)\sin(\beta_i - 2\beta_j) \end{aligned} \tag{2.21}$$

As it seen in the equations above, values of the constants depend on the coordinates of the i^{th} control point and the j^{th} boundary point of the panels; also, the orientation angles of both i^{th} and j^{th} panels.

$$Cn1_{ii} = -1 \text{ and } Cn2_{ii} = 1 \tag{2.22}$$

2.2.5. Establishing Right Hand Side Vector

Since the Eq. 2.5 (Kutta Condition) is added to the set of linear equations above, there will be m+1 unknowns and m+1 equations; accordingly, let's rearrange the equations in generalized form:

$$\sum_{j=1}^{m+1} An_{ij}\gamma_j = RHS_i \qquad i = 1,2,...,m+1 \tag{2.23}$$

where, for $i<m+1$:

$$\begin{aligned} &An_{i1} = Cn1_{i1} \\ &An_{ij} = Cn1_{ij} + Cn2_{ij-1}; \qquad j = 2,\ 3,\ \ldots\ , m \\ &An_{im+1} = Cn2_{im} \\ &RHS_i = Q_\infty \sin(\beta_i - \alpha) \end{aligned} \tag{2.24}$$

for $i=m+1$:

$$\begin{aligned} &An_{i1} = An_{im+1} = \frac{1}{2\pi} \\ &An_{ij} = 0; \qquad\qquad j = 2,\ 3,\ \ldots\ , m \\ &An_{im+1} = Cn2_{im} \\ &RHS_i = 0 \end{aligned} \tag{2.25}$$

2.2.6. Solution of Linear Set of Equations

After solution of the Eq. 2.23 by linear algebra, unknown vortex strengths are obtained. Accordingly, the total tangential velocity and pressure at each control point can be found as:

$$Q_{t_i} = Q_\infty \cos(\beta_i - \alpha) + \sum_{j=1}^{m} \left(Ct1_{ij}\gamma_j + Ct2_{ij}\gamma_{j+1} \right) \qquad i = 1,2,...,m \tag{2.26}$$

Where;

$$
\begin{aligned}
Ct1_{ij} &= \left(0.5CF - DG\right) - \frac{1}{2\pi} Ct2_{ij} \\
Ct2_{ij} &= \frac{1}{2\pi}\left(C + 0.5PF / S_j - (AD - CE)G / S_j\right) \\
Ct1_{ii} &= Ct2_{ii} = \frac{1}{4}
\end{aligned}
\tag{2.27}
$$

2.2.7. Calculation of Velocity, Pressure and Loads

If the Eq. 2.26 is rewritten in a general form:

$$
Q_{t_i} = Q_\infty \cos(\beta_i - \alpha) + q_{t_i} \tag{2.28}
$$

Or in a more useful form:

$$
Q_{t_i} = Q_\infty \cos(\beta_i - \alpha) + \sum_{j=1}^{m+1} At_{ij}\gamma_j \qquad i = 1, 2, \ldots m \tag{2.29}
$$

Where the tangential influence coefficients are given as:

$$
\begin{aligned}
At_{i1} &= Ct1_{i1} \\
At_{ij} &= Ct1_{ij} + Ct2_{ij-1}; \qquad j = 2,\ 3,\ \ldots,\ m \\
At_{im+1} &= Ct2_{im}
\end{aligned}
\tag{2.30}
$$

The pressure coefficient at the i^{th} control point is also expressed as:

$$
C_{p_i} = 1 - \frac{Q_{t_i}^2}{Q_\infty^2} \tag{2.31}
$$

By means of Kutta-Joukowsky theorem, all vortex strengths are integrated along the body surface to obtain the total circulation around the body. Then, in this direction, the lift force per unit span and the moment per unit span; the lift and the moment coefficients can be obtained respectively (Anderson, 2016).

The total circulation is:

$$\Gamma = \sum_{j=1}^{m} \frac{\gamma_j + \gamma_{j+1}}{2} S_j \tag{2.32}$$

The lift force per unit span is expressed as:

$$L' = \rho Q_\infty \sum_{j=1}^{m} \Gamma_j \tag{2.33}$$

or in an open form:

$$L' = \rho Q_\infty \sum_{j=1}^{m} \frac{\gamma_j + \gamma_{j+1}}{2} S_j \tag{2.34}$$

The moment per unit span is given as:

$$M_0' = -\rho Q_\infty \sum_{j=1}^{m} \Gamma_j x_j \cos\beta_j \tag{2.35}$$

or in an open form:

$$M_0' = -\rho Q_\infty \sum_{j=1}^{m} \frac{\gamma_j + \gamma_{j+1}}{2} S_j (x_j \cos\beta_j) \tag{2.36}$$

The lift and the moment coefficients for an airfoil are defined as:

$$c_l = \frac{L'}{\frac{1}{2}\rho Q_\infty^2 c} \tag{2.37}$$

$$c_{m,0} = \frac{M_0'}{\frac{1}{2}\rho Q_\infty^2 c^2} \tag{2.38}$$

Finally, the lift and moment coefficients for an airfoil becomes:

$$c_l = \frac{1}{Q_\infty c} \sum_{j=1}^{m} (\gamma_j + \gamma_{j+1}) S_j \tag{2.39}$$

$$c_{m,0} = -\frac{1}{Q_\infty c^2} \sum_{j=1}^{m} (\gamma_j + \gamma_{j+1}) S_j (x_j \cos \beta_j) \tag{2.40}$$

CHAPTER 3

UNSTEADY PANEL METHOD

The Chapter 3 was mainly prepared in the light of the textbook "Low Speed Aerodynamics" (Joseph Katz and Plotkin (2001)); therefore, unless any reference in the text is given, that indicates the reference as the book. Moreover, the textbook "Foundations of Aerodynamics: Bases of Aerodynamic Design" (Kuethe & Chow, 1997) was referred for the bound panel influence calculations as well. Though, for some key points, the other sources were utilized, and their references were separately given.

The modelling of the unsteady flow is very similar to the steady flow both for analytical and numerical methods. Thus, with only several modifications in the methods, the steady state solution can be transformed to unsteady one. These modifications can be summarized as:

- Neumann boundary condition is rewritten by including kinematic velocity components
- Unsteady Bernoulli equation is used instead of steady Bernoulli.
- Wake model is implemented in the light of "complementary physical conditions"

The first two can be considered as very minor and local modifications. Though, the third is more challenging; for this one, the vortex singularity element was preferred to model the wake. In the Fig. 11, the updated flow chart for the unsteady flow problem is given.

3.1. Fundamentals of the Unsteady Incompressible Flow Dynamics

The formulation of the unsteady incompressible flow dynamics is more elaborate and detailed; since, in this chapter, necessary concepts were briefly discussed. For further details, the reference text book can be referred. In the section 3.1. the fundamental concepts and mathematics were introduced, the key points of the Model 2 were discussed in the section 3.2.

3.1.1. Coordinate Systems and Formulation of the Dynamics

In the first (steady) model, the body fixed frame of reference was enough for the modelling of the flow. However, to formulate the unsteady flow dynamics, in addition to the body fixed frame, the inertial frame of reference must also be established. These coordinate systems were shown in the Fig. 8. In here, the upper and lower cases indicate the inertial and the body coordinate systems respectively:

$$\mathbf{R}(t) = (X, Y, Z) \tag{3.1}$$

$$\mathbf{r}(t) = (x, y, z) \tag{3.2}$$

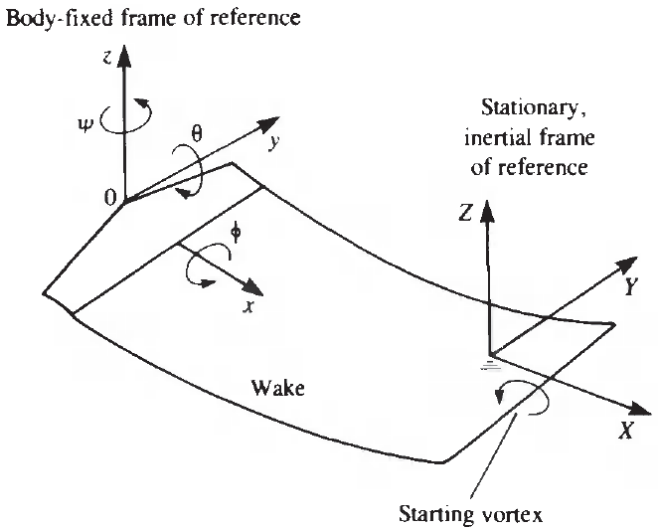

Figure 8. Inertial and body frame of references for the unsteady flow problem (Source: J. Katz and Plotkin (1991))

To simplify the calculations, the relation between the two coordinate systems are prescribed such that, at the *t=0*, body and inertial frames are coincident; and at *t>0*, motion of the origin of the body frame relative to the inertial frame starts. The relative motion of the body origin and orientation at t moment are represented by $\mathbf{R}_0(t)$ and $\Theta(t)$ respectively:

$$\mathbf{R}_0(t) = (X_0, Y_0, Z_0) \tag{3.3}$$

$$\Theta(t) = (\phi, \theta, \psi) \tag{3.4}$$

It is useful to transform the fundamental equations which are written in the inertial frame of reference for the unsteady problem to the body-fixed frame of reference. General relation between the two coordinate systems can be expressed as:

$$\begin{pmatrix} x \\ y \\ z \end{pmatrix} = f(X_0, Y_0, Z_0, \phi, \theta, \psi) \begin{pmatrix} X \\ Y \\ Z \end{pmatrix} \tag{3.5}$$

The details of the transformations between the inertial and body frames can be found in any basic dynamics textbook and for now have been skipped. The equation for the kinematic velocity of the surface in the body frame which is due to the motion of the body is expressed as:

$$\mathbf{v} = -[\mathbf{V_0} + \mathbf{v_{rel}} + \mathbf{\Omega} \times \mathbf{r}] \tag{3.6}$$

If the components are explained, $\mathbf{V_0}$, $\mathbf{\Omega} \times \mathbf{r}$ and $\mathbf{v_{rel}}$ are stated as the translational, rotational and relative (small amplitude oscillation, vibration etc.) velocities respectively:

$$\mathbf{V_0} = (\dot{X}_0, \dot{Y}_0, \dot{Z}_0) \tag{3.7}$$

$$\mathbf{\Omega} = (\dot{\phi}, \dot{\theta}, \dot{\psi}) \tag{3.8}$$

$$\mathbf{v_{rel}} = (\dot{x}, \dot{y}, \dot{z}) \tag{3.9}$$

In this direction, if the fundamental equations are written in body frame:

Laplace equation:

$$\nabla^2 \Phi = 0 \qquad (in\ x,\ y,\ z\ coordinates) \tag{3.10}$$

Zero normal flow boundary condition:

$$(\nabla \Phi + \mathbf{v}) \bullet \mathbf{n} = 0 \qquad (in\ x,\ y,\ z\ coordinates) \tag{3.11}$$

or in an open form:

$$(\nabla\Phi - \mathbf{V_0} - \mathbf{v_{rel}} - \boldsymbol{\Omega}\times\mathbf{r})\bullet\mathbf{n} = 0 \qquad (in\ x,\ y,\ z\ coordinates) \tag{3.12}$$

If the general integral equation for the unsteady flow problem is expressed:

$$\left\{\frac{1}{4\pi}\int_{Body+Wake}\mu\nabla\left[\frac{\partial}{\partial n}\left(\frac{1}{r}\right)\right]dS - \frac{1}{4\pi}\int_{Body}\sigma\nabla\left(\frac{1}{r}\right)dS - \mathbf{V_0} - \mathbf{v_{rel}} - \boldsymbol{\Omega}\times\mathbf{r}\right\}\bullet\mathbf{n} = 0 \tag{3.13}$$

3.1.2. Complementary Physical Conditions

To find a unique solution for the flow problem, the strength and the shape of the wake must be obtained. The physical conditions are the *complementary concepts* for the flow problem. Let's start with conditions regarding *the strength of the wake*:

The first one is the Kutta condition which dictates that the circulation at the trailing edge is zero:

$$\gamma_{T.E.} = 0 \tag{3.14}$$

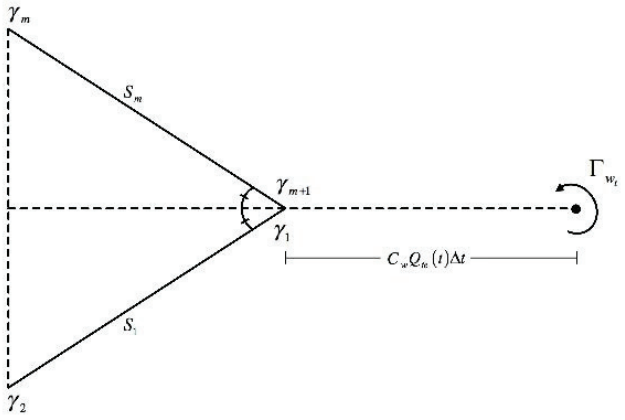

Figure 9. Shedding wake vortex in the sense of the bisector line of the trailing edge angle at time *t*

The second and new condition is the Kelvin condition which states that the total amount of circulation in a closed fluid domain is conserved by the time:

$$\frac{d\Gamma}{dt} = 0 \tag{3.15}$$

After these two conditions above, now *the shape of the wake* can be stated. The Kutta-Joukowski theorem dictates that:

$$\mathbf{Q} \times \gamma_W = 0 \tag{3.16}$$

From this point of view, it can be concluded that:

$$\mathbf{Q} \parallel \gamma_W \tag{3.17}$$

Most of the time, as shown in the Fig. 9, it is a good approximation that the wake vortex sheds on the point the which is in the sense of the bisector of the trailing edge.

3.2. Unsteady Panel Method

3.2.1. Choice of Singularity Element

In the unsteady model, as it is stated in the first (steady) model, the planar vortex panels were used to model the bound (body) part. Accordingly, same equations, coefficients etc. for the bound part will also be benefited in the new model again.

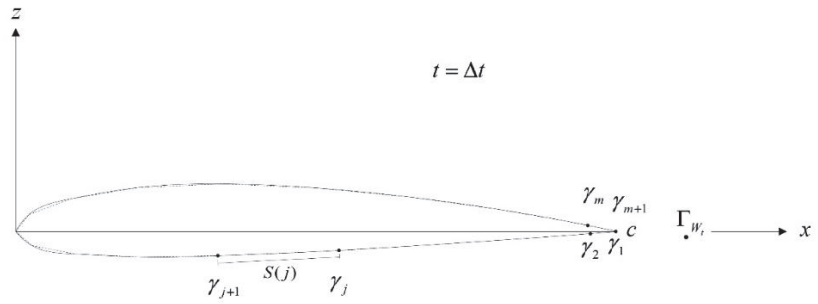

Figure 10. The planar and the point vortices on the flow domain at *t=Δt*.

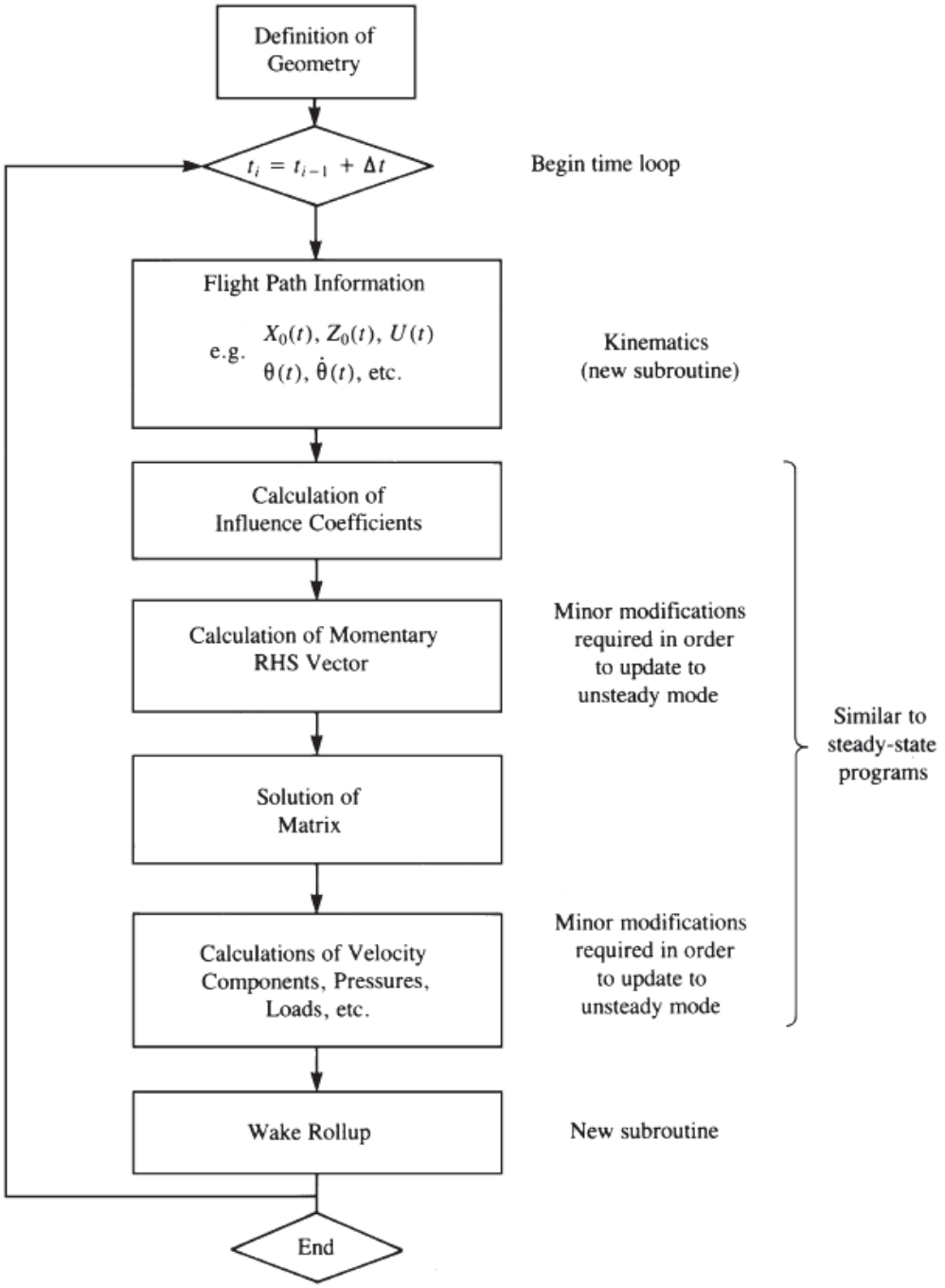

Figure 11. General flow chart of the unsteady problem
(Source: Joseph Katz and Plotkin (2001))

Though, for the wake part, the point vortices were used in terms of effective wake rollup modelling. (Shown in Fig. 10) Therefore, the new influence for the point vortex is introduced:

$$\begin{pmatrix} u \\ w \end{pmatrix} = \frac{\Gamma_j}{2\pi r_j^2} \begin{pmatrix} 0 & 1 \\ -1 & 0 \end{pmatrix} \begin{pmatrix} x - x_j \\ z - z_j \end{pmatrix} \tag{3.18}$$

where

$$r_j^2 = (x - x_j)^2 + (z - z_j)^2 \tag{3.19}$$

In here, x_j and z_j and x, z are the coordinates of the point vortex Γ_j and the arbitrary point respectively; u and w are the velocities which are induced by the element in the body frame.

3.2.2. Kinematics of the Flow

The flight path and the orientation of the body-fixed coordinate system according to the inertial frame is given as:

$$X_0 = X_0(t) \quad Z_0 = Z_0(t) \quad \theta = \theta(t) \tag{3.20}$$

Moreover, the rotation of the frame about the y axis and instantaneous velocity components of the origin:

$$\dot{X}_0 = \dot{X}_0(t) \quad \dot{Z}_0 = \dot{Z}_0(t) \quad \dot{\theta} = \dot{\theta}(t) \tag{3.21}$$

In the unsteady model, three different type of motions -*sudden forward, heaving and pitching*- were formulated.

- The first motion is the sudden forward motion of a body which flies at the constant speed of Q_∞ in -X direction is also expressed as:

$$\begin{aligned} X_0 &= -Q_\infty t & \dot{X}_0(t) &= -Q_\infty \\ Z_0 &= 0 & \dot{Z}_0(t) &= 0 \\ \theta &= \alpha_3 & \dot{\theta} &= 0 \end{aligned} \tag{3.22}$$

Where α_3 represents the constant angle of attack in radian.

- Secondly, consider a body which performs a heaving oscillation at a radial frequency of ω_2 during it flies at the constant speed of Q_∞ in -X direction

$$
\begin{aligned}
X_0 &= -Q_\infty t & \dot{X}_0(t) &= -Q_\infty \\
Z_0 &= -h_2 \sin \omega_2 t & \dot{Z}_0(t) &= -h_2 \omega_2 \cos \omega_2 t \\
\theta &= 0 & \dot{\theta} &= 0
\end{aligned} \tag{3.23}
$$

Where, h_2 is the dimensionless heaving amplitude.

- Final motion is such that the body performs a pitching oscillation at a radial frequency of ω_1 around the y axis which is in the pitching axis on the chord line during it flies at the constant speed of Q_∞ in -X direction

$$
\begin{aligned}
\theta &= \theta_m + \theta_a \sin \omega_1 t & \dot{\theta} &= \theta_a \omega_1 \cos \omega_1 t \\
X_0 &= -Q_\infty t - l_{pa} \cos \theta & \dot{X}_0(t) &= -Q_\infty + l_{pa} \dot{\theta} \sin \theta \\
Z_0 &= l_{pa} \sin \theta & \dot{Z}_0(t) &= l_{pa} \dot{\theta} \cos \theta
\end{aligned} \tag{3.24}
$$

Where θ_m, θ_a are the mean and amplitude angles in radian; and l_{pa} is the location of the pitching axis which is in the hundredths of chord respectively.

If the relation between the coordinate systems shown in the Fig. 8 is expressed:

$$
\begin{pmatrix} X \\ Z \end{pmatrix} = \begin{pmatrix} \cos\theta(t) & \sin\theta(t) \\ -\sin\theta(t) & \cos\theta(t) \end{pmatrix} \begin{pmatrix} x \\ z \end{pmatrix} + \begin{pmatrix} X_0 \\ Z_0 \end{pmatrix} \tag{3.25}
$$

Furthermore, the transformed velocities are:

$$
\begin{pmatrix} \dot{X} \\ \dot{Z} \end{pmatrix} = \begin{pmatrix} \cos\theta(t) & \sin\theta(t) \\ -\sin\theta(t) & \cos\theta(t) \end{pmatrix} \begin{pmatrix} \dot{x} \\ \dot{z} \end{pmatrix} \tag{3.26}
$$

By using the inverse transformation, it is also meaningful to introduce the velocity components, U_t and W_t observed in the x, z frame of reference:

$$
\begin{pmatrix} U_t \\ W_t \end{pmatrix} = \begin{pmatrix} \cos\theta(t) & -\sin\theta(t) \\ \sin\theta(t) & \cos\theta(t) \end{pmatrix} \begin{pmatrix} -\dot{X}_0 \\ -\dot{Z}_0 \end{pmatrix} \tag{3.27}
$$

3.2.3. Meshing Geometry

The orientation angle β_i is defined as in the clockwise direction in the trigonometric system. In this context, the normal and tangential unit vectors were expressed as:

$$\mathbf{n}_i = \frac{\left(-\frac{dz}{dx}, 1\right)}{\sqrt{\left(\frac{dz}{dx}\right)^2 + 1}} = (-\sin\beta_i, \cos\beta_i) \tag{3.28}$$

$$\boldsymbol{\tau}_i = (\cos\beta_i, \sin\beta_i) \tag{3.29}$$

Discretization of the body is the same as specified in the model 1.

3.2.4. Computation of Influence Coefficients

Before starting the calculation of the influence coefficients, the time loop must be created. In this way, the momentary time is defined as:

$$t = I_t \cdot \Delta t \tag{3.30}$$

Where, I_t is the time step counter and Δt is the time step. At the $t=0$, the body is stationary, and the body-fixed and inertial coordinate systems are coincided.(For pitching motion only the x and X are coincided) For $t>0$ or in other words $I_t>0$, body starts to motion and at the momentary time $t=\Delta t$, the first wake vortex Γ_{W_1} is shed. The location of the wake vortex Γ_{W_t} at time t is where is far from the trailing edge at 0.2-0.3 of the distance travelled by the trailing edge during the latest time step. By means of the transformation given in the 3.2.2., the location of the trailing edge by the time can be obtained.

To calculate the influence coefficients, the Neumann boundary condition (the zero-normal flow across the solid body) was applied on each collocation (control) point. The normal velocity component on the collocation point is composed of self-induced, kinematic, and wake-induced velocity components. The self-induced velocity is

calculated almost same as in the steady part. The kinematic velocity which is due to the airfoil motion relative to the inertial frame is known and is written in the right-hand side of the equation by using the transformations which have been given in the section 3.2.2. Kutta condition is also applied at the trailing edge of the body same as in the steady part. Regarding to the wake induced part, at the momentary time *t*, the most recent wake vortex is unknown, and its influence on each collocation point is written in the influence coefficient matrix; the strength of circulation is calculated by means of Kelvin condition. However, the wake vortices which were induced in the previous time steps are known; since, their influences on each collocation point are transferred to the right-hand side of equation.

The perturbation potential in the momentary boundary condition which was given in the Eq. 3.12 can be split into bound and wake potentials in terms of useful representation and accordingly the equation can be expressed in the form:

$$(\nabla\Phi_B + \nabla\Phi_W - \mathbf{V_0} - \mathbf{v_{rel}} - \mathbf{\Omega}\times\mathbf{r})\bullet\mathbf{n} = 0 \qquad (in\ x,\ y,\ z\ coordinates) \qquad (3.31)$$

The normal component of the self-induced velocity at collocation point #1 which is created by the m bound *panels* and the most recent wake vortex Γ_{W_t} is written as follows:

$$q_{n1} = An_{11}\gamma_1 + An_{12}\gamma_2 + An_{13}\gamma_3 + ... + An_{1m+1}\gamma_{m+1} + An_{1m+2}\Gamma_{W_t} \qquad (3.32)$$

If the zero normal flow condition that is expressed in the Eq. (3.31) is formulated for each collocation point, the equation becomes:

$$An_{i1}\gamma_1 + An_{i2}\gamma_2 + An_{i3}\gamma_3 + ... + An_{im+1}\gamma_{m+1} + An_{im+2}\Gamma_{W_t} + \left[U(t)+u_w, W(t)+w_w\right]\bullet\mathbf{n}_i = 0 \qquad (3.33)$$

In here, $[U(t),W(t)]_i$ and $[u_w, w_w]_i$ are the *u* and *w* components of the kinematic velocity and velocity induced by the wake vortices which were shed in the previous time steps.

$$\begin{pmatrix} U(t) \\ W(t) \end{pmatrix} = \begin{pmatrix} \cos\theta(t) & -\sin\theta(t) \\ \sin\theta(t) & \cos\theta(t) \end{pmatrix} \begin{pmatrix} -\dot{X}_0 \\ -\dot{Z}_0 \end{pmatrix} + \begin{pmatrix} -\dot{\theta}\eta \\ \dot{\theta}\eta - \dfrac{\partial\eta}{\partial t} \end{pmatrix} \qquad (3.34)$$

The momentary kinematic velocity components were given in the Eq. (3.34). The first and second matrices of the equation are the translational and the rotational parts respectively. Since the small-amplitude motions (vibration etc.) are not in the scope of this study, the $\frac{\partial n}{\partial t}$ term was neglected. As it was stated above, the known *u* and *w* components of the kinematic and wake induced velocity terms which were transferred to the right-hand side and are expressed as in the form:

$$RHS_i = -\left[U(t) + u_w, W(t) + w_w\right] \bullet \mathbf{n}_i \tag{3.35}$$

The tangential component of the self-induced velocity at each collocation point is equal to the derivation of the perturbation potential with respect to the tangential unit vector:

$$\frac{\partial \Phi}{\partial \boldsymbol{\tau}_i} = q_{t_i} \tag{3.36}$$

Thus, it is equal to the summation of the influences by *m bound panels*. If the tangential component of the self-induced velocity at collocation point *#1* is written:

$$q_{t_1} = At_{11}\gamma_1 + At_{12}\gamma_2 + At_{13}\gamma_3 + ... + At_{1m+1}\gamma_{m+1} \tag{3.37}$$

The Kutta condition which dictates that the total circulation at the trailing edge is zero is stated same as in the steady state solution (discussed in Chapter 2):

$$\gamma_1 + \gamma_{m+1} = 0 \tag{2.5}$$

To compute the strength of the most recent wake vortex Γ_{W_t}, the Kelvin Condition which states that the amount of total circulation in a closed fluid domain is conserved with respect to time is written as the last equation in that form:

$$\Gamma(t) + \Gamma_{W_t} = \Gamma(t - \Delta t) \tag{3.38}$$

Where, $\Gamma(t)$ is the momentary total bound circulation and is given as:

$$\Gamma(t) = \sum_{j=1}^{m} \frac{\gamma_j + \gamma_{j+1}}{2} S_j \tag{3.39}$$

Finally, the algebraic set of equations is expressed in matrix form in the Eq. (3.40) below:

$$\begin{bmatrix} An_{11} & An_{12} & \dots & An_{1m} & An_{1m+1} & An_{1m+2} \\ An_{21} & An_{22} & \dots & An_{2m} & An_{2m+1} & An_{2m+2} \\ \dots & \dots & \dots & \dots & \dots & \dots \\ An_{m1} & An_{m2} & \dots & An_{mm} & An_{mm+1} & An_{mm+2} \\ 1 & 0 & \dots & 0 & 1 & 0 \\ S_1 & (S_1+S_2)/2 & \dots & (S_{m-1}+S_m)/2 & S_m & 1 \end{bmatrix} \begin{bmatrix} \gamma_1 \\ \gamma_2 \\ \dots \\ \gamma_m \\ \gamma_{m+1} \\ \Gamma_{W_t} \end{bmatrix} = \begin{bmatrix} RHS_1 \\ RHS_2 \\ \dots \\ RHS_m \\ 0 \\ \Gamma(t-\Delta t) \end{bmatrix} \tag{3.40}$$

If it is summarized, except the last row and column, the normal influence coefficients are identical with the steady state ones. The last row is the Kelvin condition and last column (until the element *#m*) is the normal influence coefficients by the latest wake vortex. The unknown circulation strengths are computed by linear algebra.

3.2.5. Establishing RHS Vector

$$\sum_{j=1}^{m+2} An_{ij}(\dots)_j = RHS_i \quad i = 1,2,\dots,m+2 \tag{3.41}$$

where

$$RHS_i = -\left[U(t)+u_w, W(t)+w_w\right] \bullet \mathbf{n}_i \tag{3.35}$$

3.2.6. Solve Linear Set of Equations

$$(\dots)_j = \sum_{j=1}^{m+2} An_{ij}^{-1} RHS_i \tag{3.42}$$

3.2.7. Computation of Velocity Components, Pressures and Loads

Since the problem is time-dependent, the unsteady Bernoulli equation is used in the pressure calculations:

$$\frac{p_{ref} - p}{\rho} = \frac{Q^2}{2} - \frac{v_{ref}^2}{2} + \frac{\partial \Phi}{\partial t} \tag{3.43}$$

Where, p_{ref} and p are the pressure values at the reference point(freestream) and the point of interest respectively. Reference velocity v_{ref} is the magnitude of the time dependent kinematic velocity and Q is the total velocity. $\frac{\partial \Phi}{\partial t}$ component represents the rate of change of perturbation potential along a streamline with respect to time. Before writing them in open forms, let's express the unsteady Bernoulli equation for each collocation point:

$$p_i = \rho\left(\frac{v_{ref_i}^2}{2} - \frac{Q_i^2}{2} - \frac{\partial \Phi_i}{\partial t}\right) + p_{ref} \tag{3.44}$$

Reference velocity v_{ref_i} is the magnitude of the time dependent kinematic velocity. Thus, is stated as:

$$v_{ref_i}^2 = U_i^2(t) + W_i^2(t) \tag{3.45}$$

Total velocity is the magnitude of the normal and the tangential components:

$$Q_i^2 = Q_{n_i}^2 + Q_{t_i}^2 \tag{3.46}$$

Since the Neumann boundary condition dictates that the total normal velocity at each collocation point is zero, the total velocity becomes equal to the total tangential velocity. Accordingly, if the tangential component is invoked in the Eq. (3.46):

$$Q = Q_{t_i} \tag{3.47}$$

The total tangential velocity equals to the freestream and perturbation components respectively; note that, the wake influences are represented in the freestream component either:

$$Q_{t_i} = [U(t) + u_w, W(t) + w_w]_i \bullet \boldsymbol{\tau}_i + \frac{\partial \Phi}{\partial \boldsymbol{\tau}_i} \tag{3.48}$$

Recalling the Eq. (2.29), tangential perturbation component is implemented in the Eq. (3.48):

$$Q_{t_i} = [U(t) + u_w, W(t) + w_w]_i \bullet \boldsymbol{\tau}_i + \sum_{j=1}^{m+1} At_{ij} \gamma_j \tag{3.49}$$

To find the $\frac{\partial \Phi_i}{\partial t}$, first, the perturbation velocity along the streamline must be integrated between the reference and the collocation points. Thus, remind that the fundamental equation for the perturbation potential:

$$\Phi = \int_C \mathbf{q} \bullet d\mathbf{l} \tag{3.50}$$

However, for simplicity, instead of the part that is from the reference point to collocation point, the integral is evaluated from the leading edge to collocation point. If the integral is written in numerical form and the potential is differentiated with respect to the time, two equations which are in same form but with different indices for lower and upper side of the body are obtained.

For lower side:

$$\frac{\partial \Phi_{l_i}}{\partial t} = \frac{\partial}{\partial t}\left(\sum_{k=i+1}^{lp} q_{t_k} S_k + \frac{q_{t_i} S_i}{2} \right) \tag{3.51}$$

For upper side:

$$\frac{\partial \Phi_{u_i}}{\partial t} = \frac{\partial}{\partial t}\left(\sum_{k=lp+1}^{i-1} q_{t_k} S_k + \frac{q_{t_i} S_i}{2} \right) \tag{3.52}$$

Where, *lp* is the number of the latest panel at the lower side which is adjacent to the leading edge. In here, since the integral is evaluated up to the i^{th} collocation point, the half of the i^{th} panel is considered in the integration (second term in the parenthesis). Now, by integrating the pressure along the body surface, the momentary lift, drag forces and the moment around the y axis at the leading edge per unit span can be obtained:

The momentary lift per unit span:

$$L' = -\sum_{i=1}^{m} p_i S_i \cos(\theta - \beta_i) \tag{3.53}$$

The momentary drag per unit span:

$$D' = -\sum_{i=1}^{m} p_i S_i \sin(\theta - \beta_i) \tag{3.54}$$

The momentary moment around y axis at the leading edge per unit span:

$$M_0' = -\sum_{i=1}^{m} p_i S_i (-x_i \cos\beta_i - z_i \sin\beta_i) \tag{3.55}$$

Moreover, to compute the lift, drag and moment coefficients, let's define the pressure coefficient according to the reference velocity:

$$C_{p_i} = \frac{p - p_{ref}}{\frac{1}{2}\rho v_{ref_i}^2} \tag{3.56}$$

Or in an open form:

$$C_{p_i} = 1 - \frac{Q_i^2}{v_{ref_i}^2} - \frac{2}{v_{ref_i}^2}\frac{\partial \Phi_i}{\partial t} \tag{3.57}$$

Accordingly, the momentary coefficients are expressed as follows in below:

The momentary lift coefficient:

$$c_l = -\frac{1}{c}\sum_{i=1}^{m} C_{p_i} S_i \cos(\theta - \beta_i) \tag{3.58}$$

The momentary drag coefficient:

$$c_d = -\frac{1}{c}\sum_{i=1}^{m} C_{p_i} S_i \sin(\theta - \beta_i) \tag{3.59}$$

The momentary moment coefficient:

$$c_{m,0} = -\frac{1}{c^2}\sum_{i=1}^{m} C_{p_i} S_i (-x_i \cos\beta_i - z_i \sin\beta_i) \tag{3.60}$$

3.2.8. Vortex Wake Rollup

Since the wake vortices are force-free, each wake vortex moves with the effect of the total velocities on the each of them. The total velocity at an any arbitrary wake vortex point is the combination of the kinematic and induced velocities. The kinematic velocity is calculated by Eq. (3.34); the induced velocity at any arbitrary wake vortex point is the result of the bound panels and the other wake vortices in the flow field. Due to the radial symmetry, the wake vortex induces no velocity on itself (Pozrikidis, 2016). The rollup of a wake vortex at the point *l* is given as:

$$(\Delta x, \Delta z)_l = [U(t) + u, W(t) + w]_l \tag{3.61}$$

CHAPTER 4

RESULTS AND DISCUSSION

4.1. Steady Model

The results of lift coefficient variations w.r.t. angle of attack of four different types of airfoil which were obtained by the current model; inviscid and viscous modes of the Xfoil program(Drela, 2001), experimental archive of the NASA(Ira H Abbott, Von Doenhoff, & Stivers Jr, 1945) were compared.

Firstly, before presentation of these results, the pressure coefficient distributions which were obtained by the current model and another numerical model from the literature (Anderson (2016)) for the NACA0012 at $\alpha=9^{o}$ were compared. The pressure coefficient distributions were shown in Fig. 12 and 13 respectively. The current model shows a well agreement with the numerical model in the literature which has the same methodology with this study for the given specific conditions.

Since the Fig. 14 is evaluated, it is seen that there are the slight differences between the Xfoil inviscid and the current model analyses for the lift coefficient of NACA0012. In here, the current model has the slightly closer values to the experimental data than the Xfoil inviscid mode. The viscous mode of the Xfoil is considerably successful in terms of the reflection of the variation at high angles of attack. The second type of airfoil 2412 has the same thickness with 0012, with a 2% difference of camber. For this profile, checking the Fig. 15, it can be said that errors among the experimental data and the inviscid models have increased compared to the first one. Furthermore, the current model is still more successful than the Xfoil inviscid mode. The analyses which were carried for the third profile 2418 shows the limitation of the viscous mode of the Xfoil (Shown in Fig. 16). The results of the current model are slightly finer than the Xfoil inviscid. For the last one, which was given in the Fig. 17, the Xfoil viscous mode did not converged to a solution at the α =10º, 12º and 14º. In addition, the Xfoil inviscid and the current model shows the identical trends. Nevertheless, in total, for these four analyses, the 2nd order vortex panel method is superior than the Xfoil inviscid model.

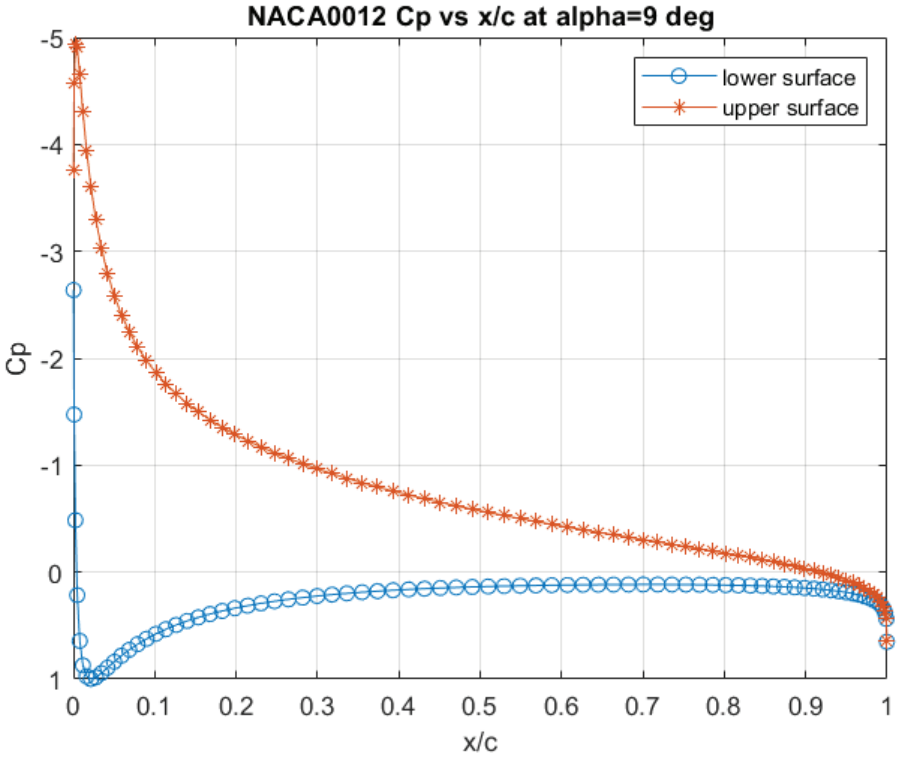

Figure 12. The analysis of the pressure coefficient distribution for the NACA0012 at $\alpha=9^{o}$

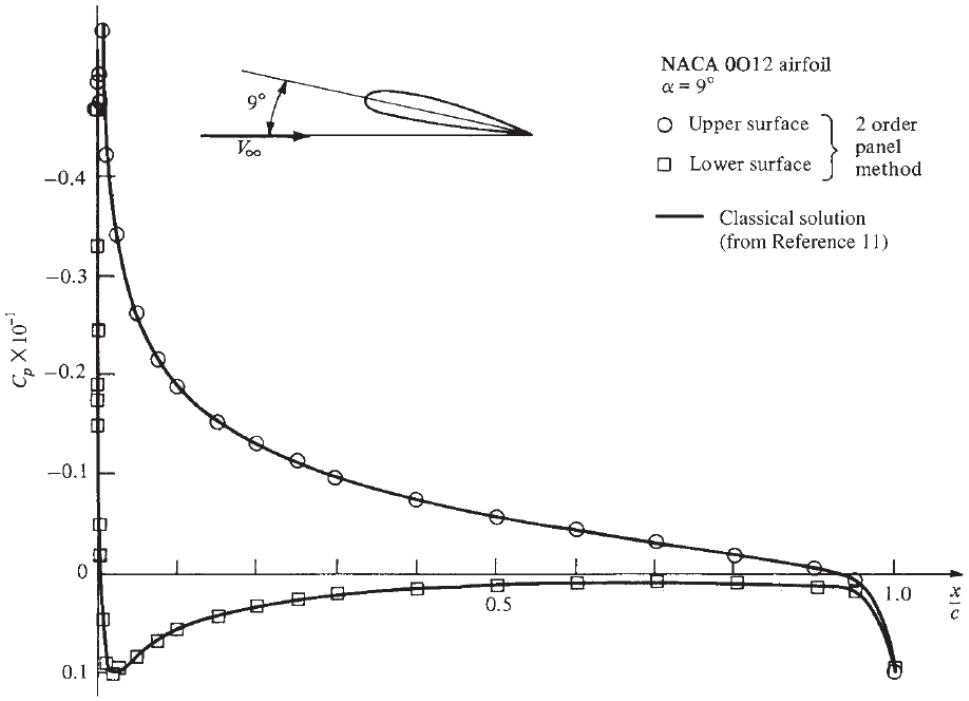

Figure 13. The analysis of the pressure coefficient distribution for the NACA0012 at $\alpha=9^{o}$ by the second order vortex panel method by Dr. Tae-Hwan Cho (Source: Anderson (2016))

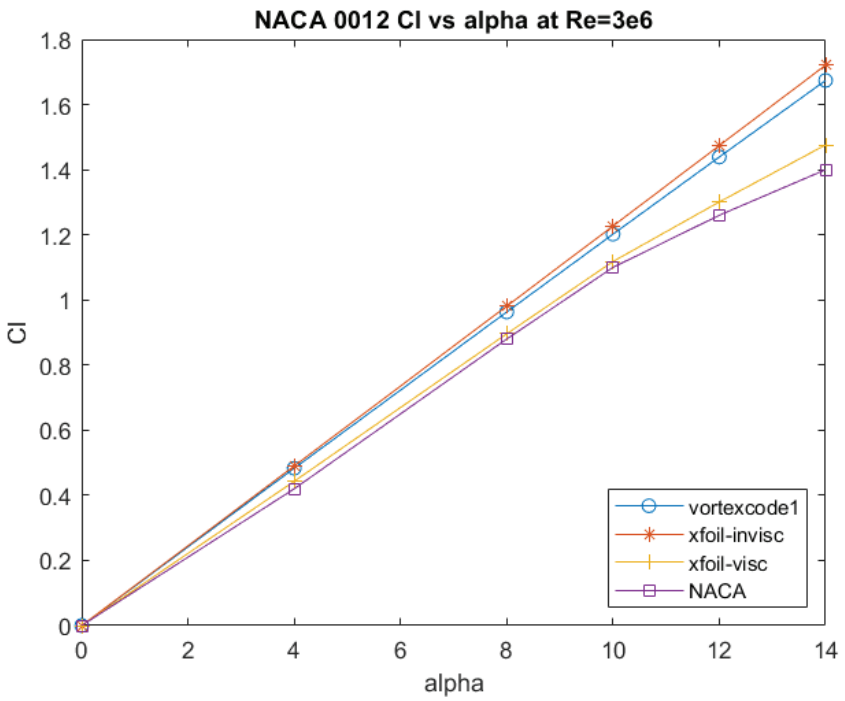

Figure 14. The lift characteristics for the NACA0012 airfoil w.r.t. angle of attack data for the Xfoil results from Drela (Source: Drela (2001)) the NACA results from Abbott et all (Source: (Ira Herbert Abbott & Von Doenhoff, 1959))

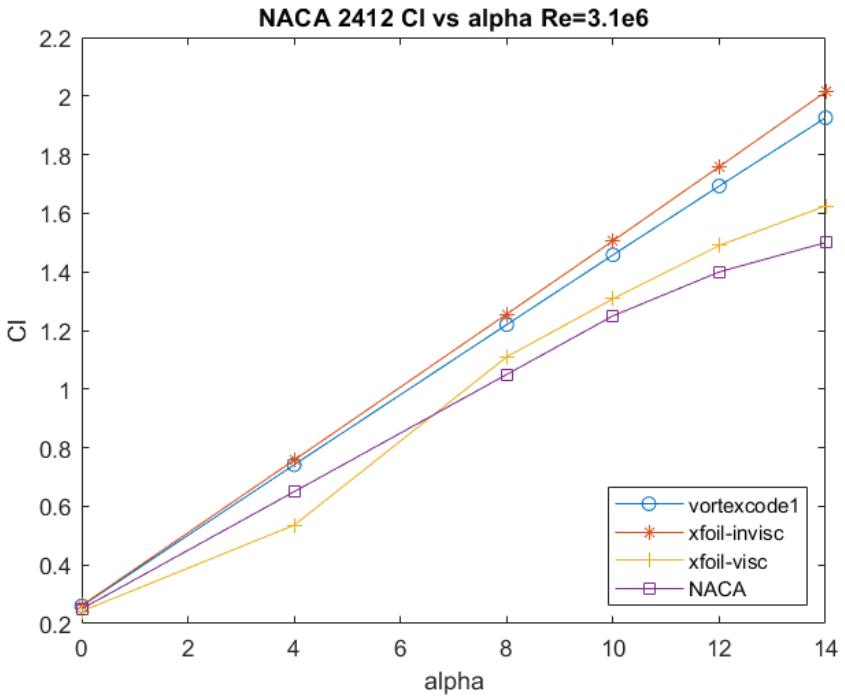

Figure 15. The lift characteristics for the NACA2412 airfoil w.r.t. angle of attack data for the Xfoil results from Drela (Source: Drela (2001)) the NACA results from Abbott et all (Source: (Ira Herbert Abbott & Von Doenhoff, 1959))

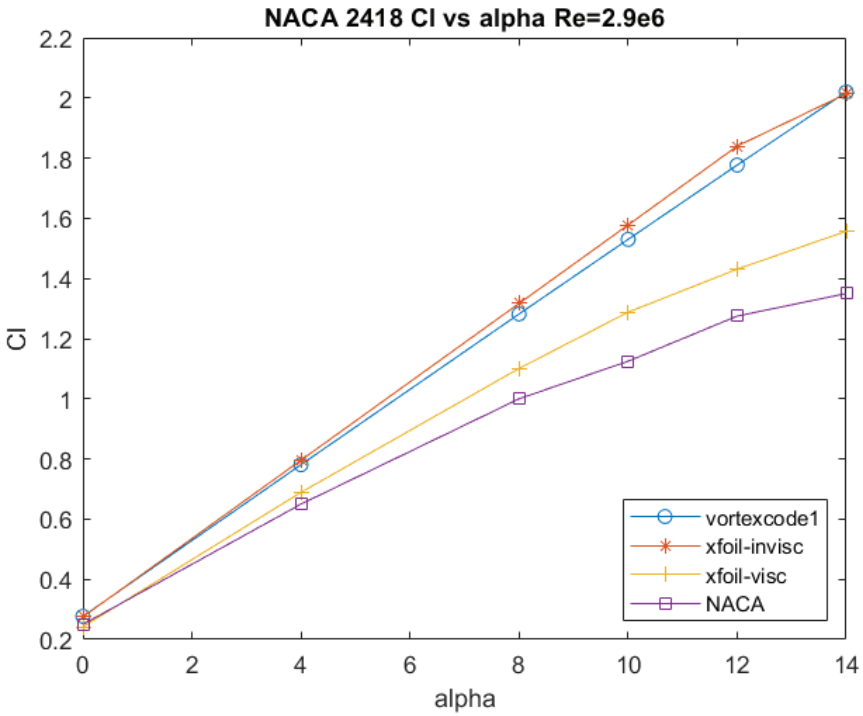

Figure 16. The lift characteristics for the NACA2418 airfoil w.r.t. angle of attack data for the Xfoil results from Drela (Source: Drela (2001)) the NACA results from Abbott et all (Source: (Ira Herbert Abbott & Von Doenhoff, 1959))

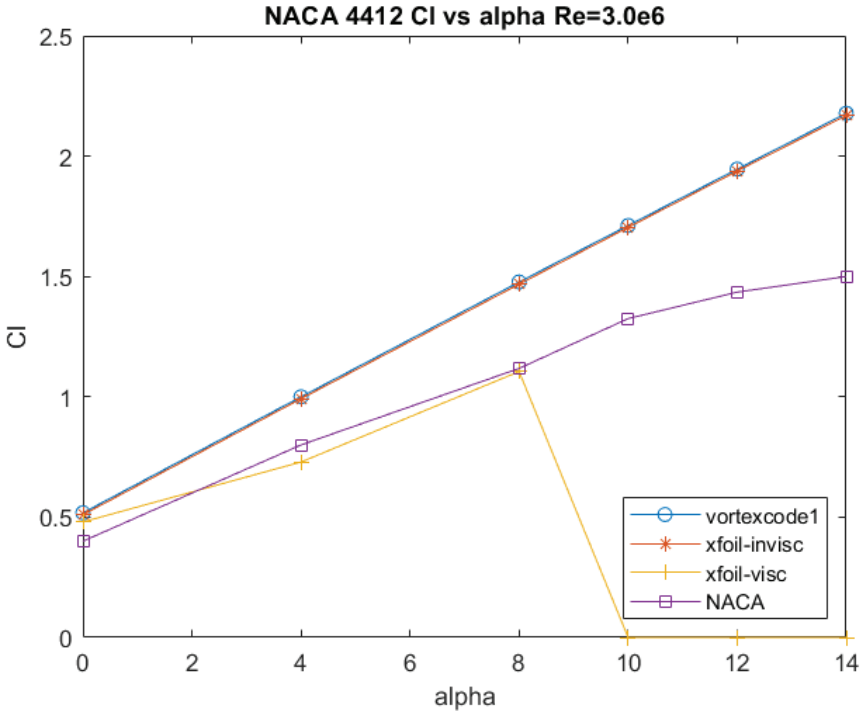

Figure 17. The lift characteristics for the NACA4412 airfoil w.r.t. angle of attack data for the Xfoil results from Drela (Source: Drela (2001)) the NACA results from Abbott et all (Source: (Ira Herbert Abbott & Von Doenhoff, 1959))

4.2. Unsteady Model

4.2.1. Sudden Forward Motion

Before starting to presentation of the results, if the Kelvin condition and the starting vortex concepts are reminded very briefly; after the starting of the body motion, the starting vortex is created at the trailing edge of the body and this vortex moves in downstream as the time passes. Consequently, by the time, the effect of the starting vortex on the body vanishes and the amount of the bound circulation increases until the steady state conditions are reached; and the amount of the total circulation in the fluid domain is conserved (Anderson (2016)). This phenomenon, which was shown in Fig. 18, is the main reason of the transient behavior of the lift and drag characteristics of the body after initiation of a sudden forward motion. Accordingly, in this part, this behavior was analyzed for two different geometries which are 2D flat plate and NACA 0012 airfoil.

The 2D flat plate case was evaluated with an exact solution by the scientist Wagner in 1925 (Wagner, 1925). The results for normalized lift $L(t)/L(t=\infty)$ and normalized circulation $\Gamma(t)/\Gamma(t=\infty)$ variations; and drag coefficient for the transient behavior which were obtained by Wagner's exact solution and lumped vortex method (Joseph Katz and Plotkin (2001)) for $U_\infty \Delta t/c=0.25$ and $\alpha=5°$ were given respectively In the Fig. 19 and 16. The analyses which were made by the current method were given In the Fig. 20 and 23. For the current method, length and the thickness of the 2D flat plate were taken as c and $0.01c$ respectively. Number of panels $m=160$ as same in the previous calculations. To prevent the creation of very large circulations around the corners of the body, the leading and trailing parts were rounded by using circular geometry. Travelling time for this analysis was chosen to be $t=1\ sec$ which was long enough to reach the steady state conditions.

If the results of Wagner are taken as the base points for the same $U_\infty \Delta t/c$ and α values, the current method is superior than the lumped vortex method in terms of reflecting the lift and circulation; and drag coefficient characteristics. There is a slight difference between the drag coefficient values at the $U_\infty t/c=10$ for the reference methods and the current method; it should be reminded that, the drag coefficient formulation of the current method is different than these two methods. Moreover, if the time step is decreased for the current method, the results for lift and circulation; and drag coefficient

characteristics which are closer to the exact solution by Wagner can be obtained. These results were shown in Fig. 21 and Fig. 24 respectively.

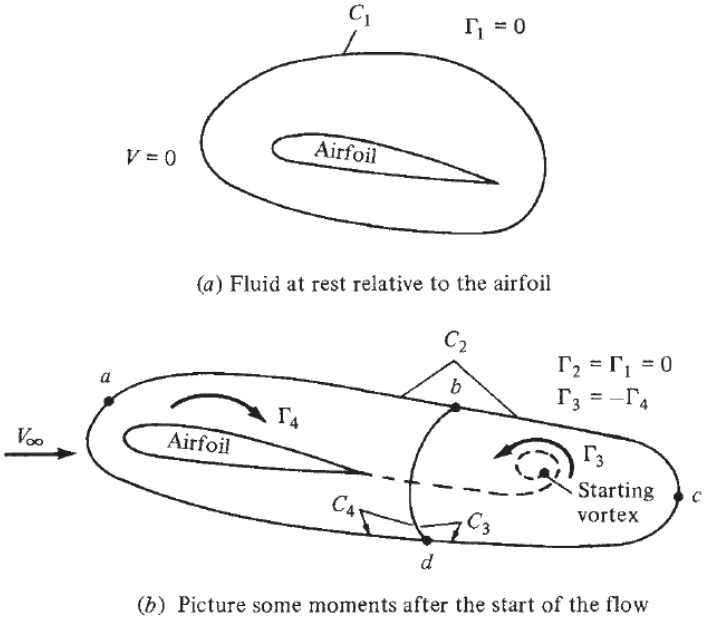

Figure 18. Representation of the Kelvin condition and the starting vortex (Source: Anderson (2016))

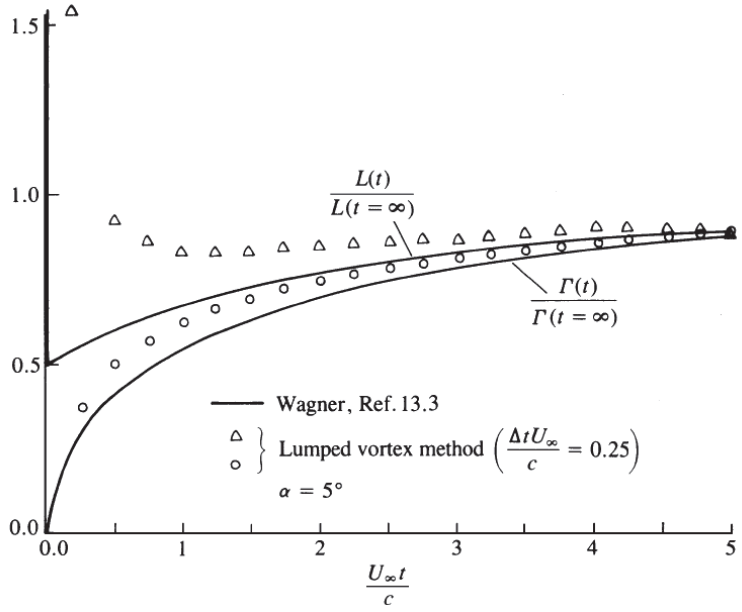

Figure 19. Lift and circulation variations w.r.t. $U_\infty t/c$ for a 2D flat plate: Comparison of the Wagner's exact solution and lumped vortex method (Source: Joseph Katz and Plotkin (2001))

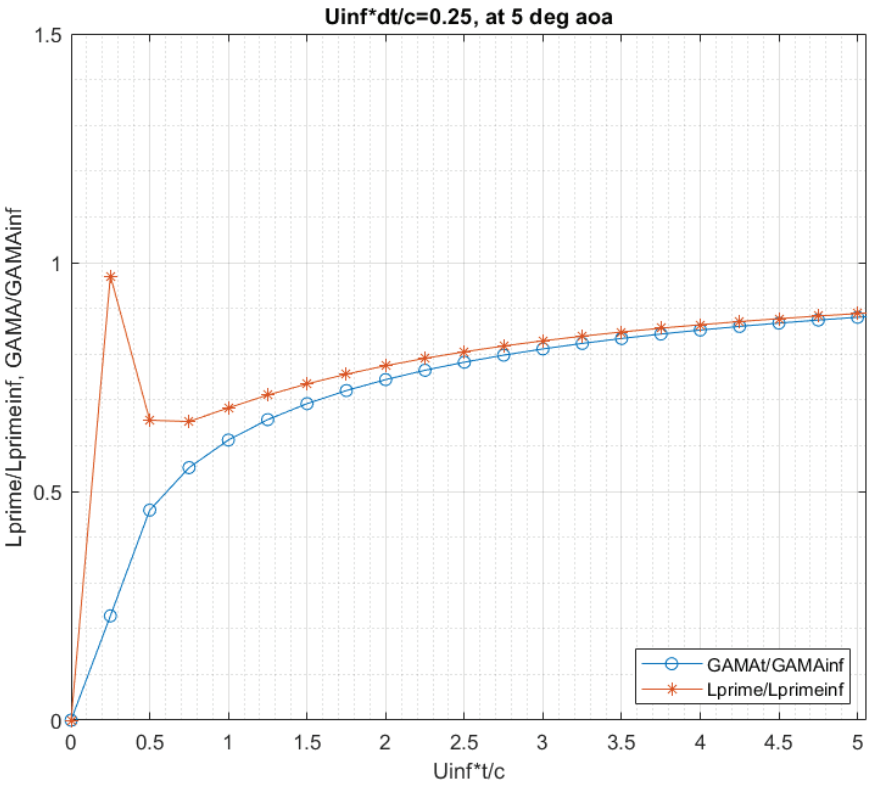

Figure 20. Lift and circulation variations w.r.t. $U_\infty t/c$ for a 2D flat plate: $U_\infty \Delta t/c=0.25$, $\alpha=5°$

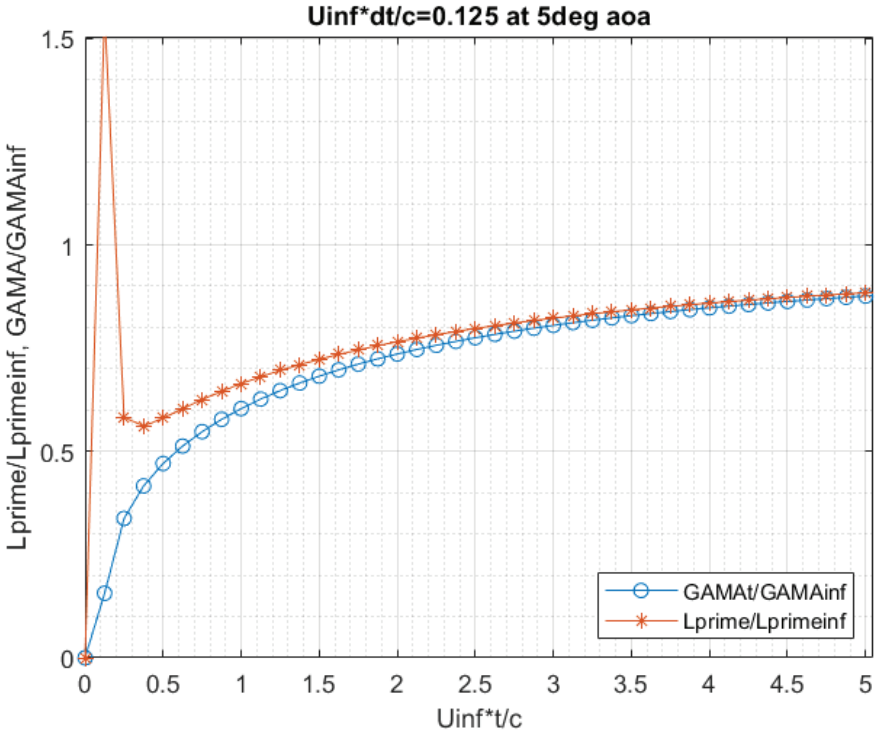

Figure 21. Lift and circulation variations w.r.t. $U_\infty t/c$ for a 2D flat plate: $U_\infty \Delta t/c=0.125$, $\alpha=5°$

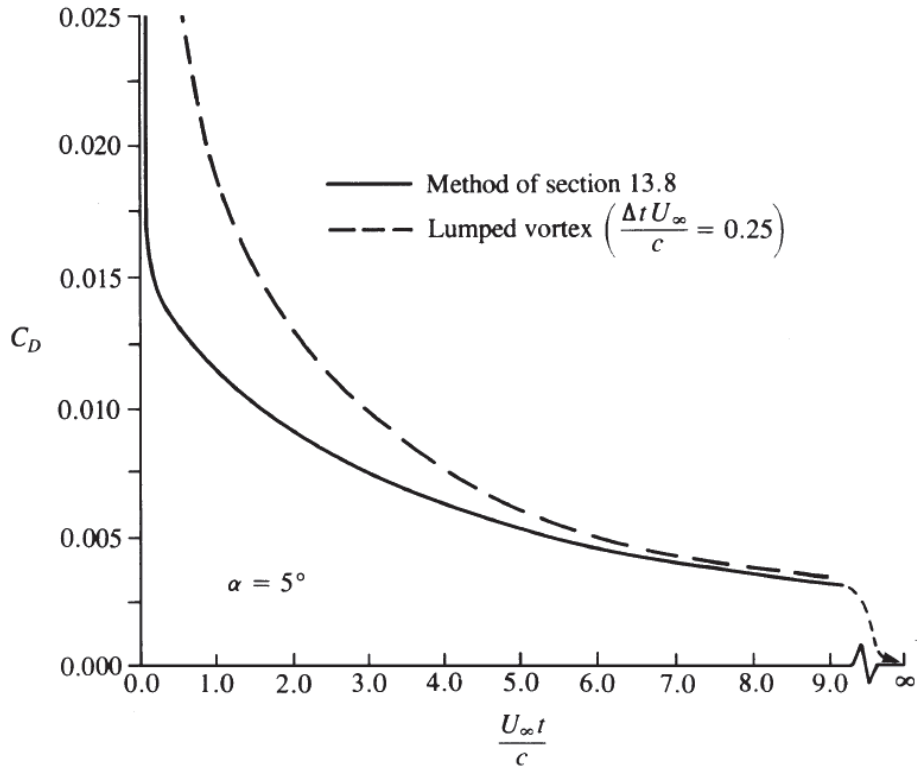

Figure 22. c_d variation w.r.t. $U_\infty t/c$ for a 2D flat plate: Comparison of the Wagner's exact solution and lumped vortex method (Source: Joseph Katz and Plotkin (2001))

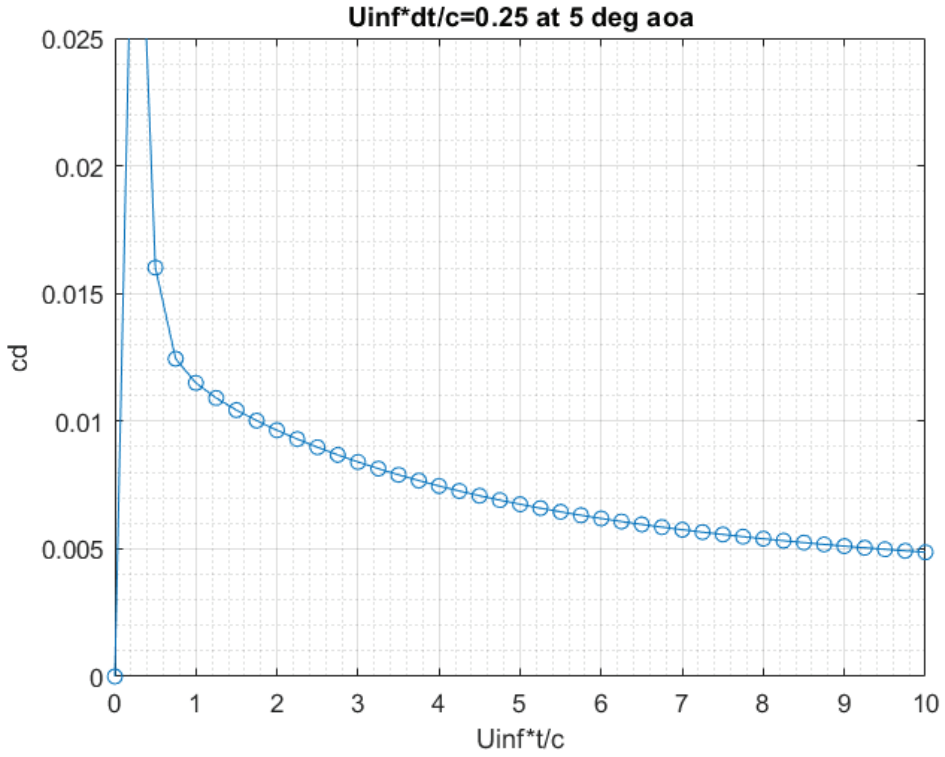

Figure 23. Drag coefficient variation w.r.t. $U_\infty t/c$ for a 2D flat plate: $U_\infty \Delta t/c=0.25$, $\alpha=5°$

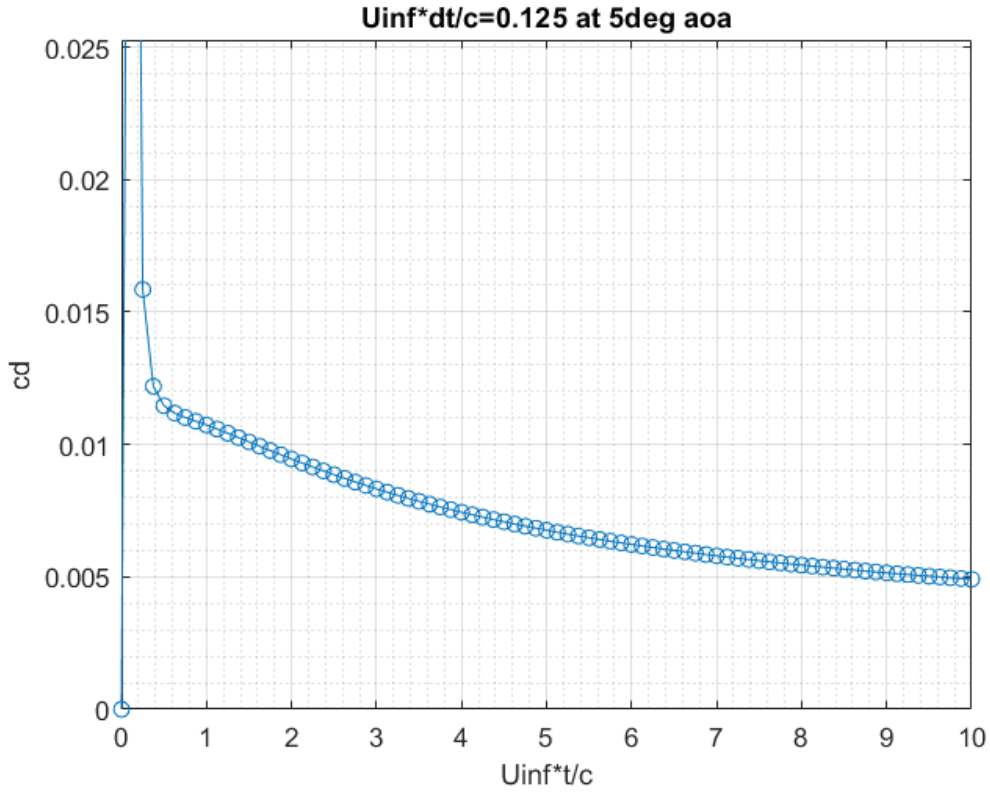

Figure 24. Drag coefficient variation w.r.t. $U_\infty t/c$ for a 2D flat plate: $U_\infty \Delta t/c=0.125$

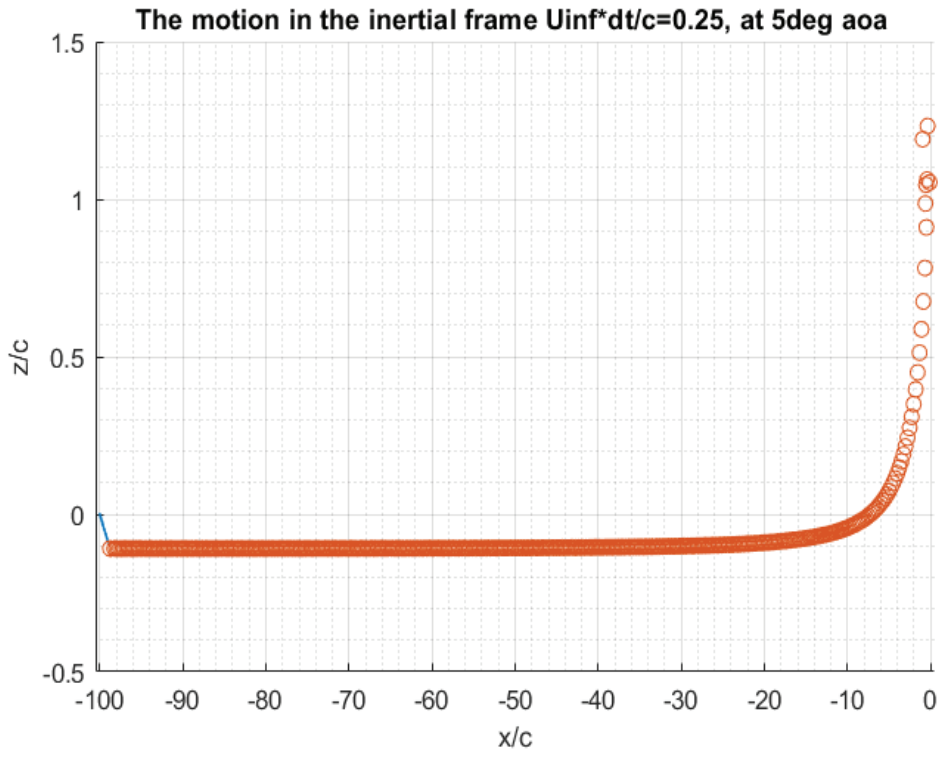

Figure 25. The motion of the 2D flat plate with the wake its behind in the inertial frame: $U_\infty \Delta t/c$=0.25, α=5°

Furthermore, the wake behind the 2D flat plate in inertial frame was also represented in the Fig. 25. In here, $U_\infty \Delta t/c=0.25$ and $\alpha=5°$ values were preferred to create the consistency. However, the travelling time was taken as *0.25 sec* (means $U_\infty t/c=0.25$) by respecting the observability. The starting vortex which was created by the sudden forward motion and moves in downstream can be seen in the right side of the figure. Furthermore, by referring the starting vortex in the Fig. 18, it can be concluded that the analyses were carried out in the accurate way.

The second geometry which is the NACA 0012 analysis was made to understand how the lift, circulation and drag characteristics could be affected by the change of the geometry. Since, for this airfoil, the results were compared with the 2D flat plate case. Keep in mind that, the NACA 0012 was chosen due to being symmetrical and having relatively small thickness compared to the other airfoils; and being commonly preferred in the literature for the analysis. The lift and circulation; and the drag characteristic analyses for the NACA 0012 airfoil profile were given in the Fig. 26 and Fig. 27 respectively. These analyses were performed for the $U_\infty \Delta t/c=0.25$, $\alpha=5°$, *t=1 sec* and *m=160* panels as the same in the flat plate case.

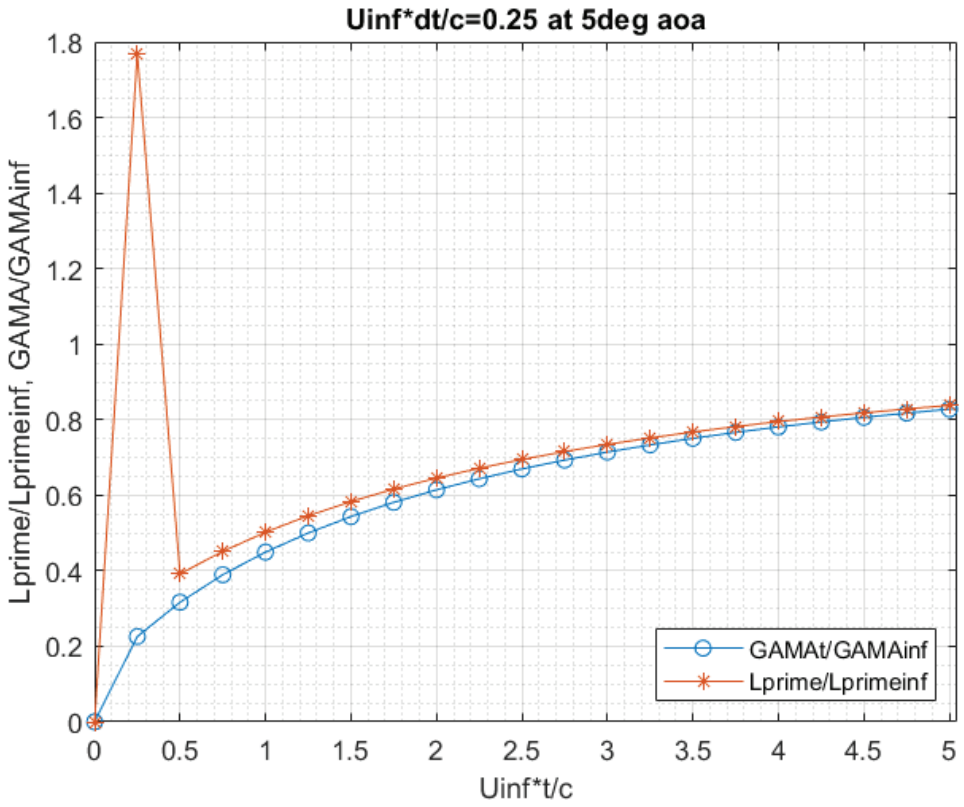

Figure 26. Lift and circulation variations w.r.t. $U_\infty t/c$ for the NACA0012: $U_\infty \Delta t/c$=0.25, α=5°

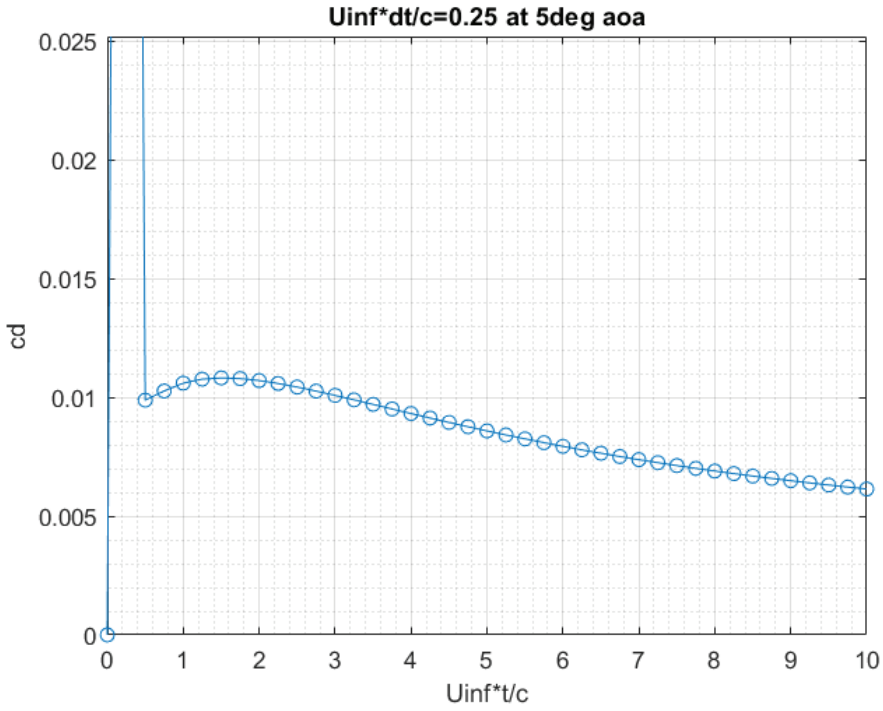

Figure 27. The drag coefficient variation w.r.t. $U_\infty t/c$ for the NACA0012: $U_\infty \Delta t/c$=0.25, α=5°

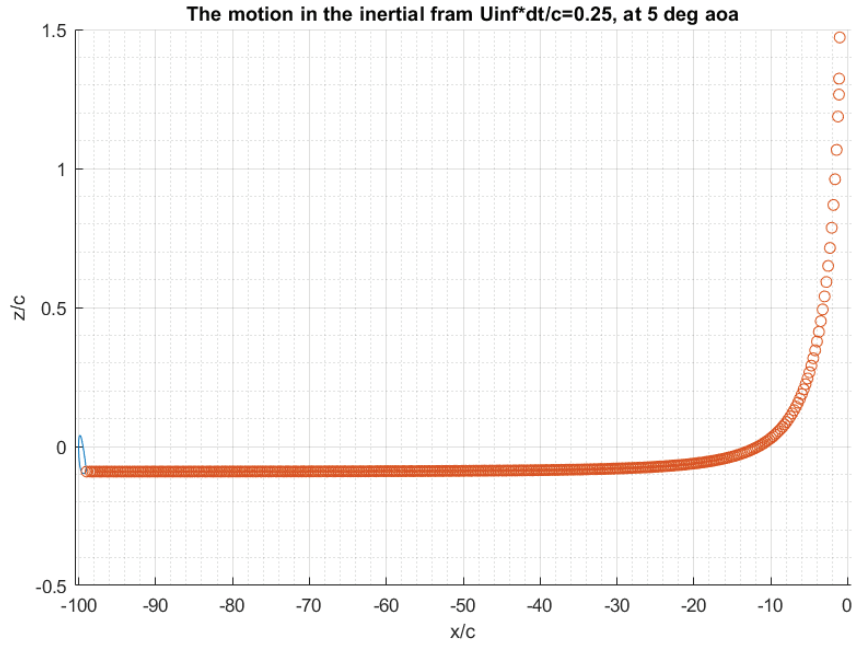

Figure 28. The motion of the NACA0012 airfoil with the wake its behind in the inertial frame: $U_\infty \Delta t/c=0.25$, α=5°

When the Fig. 20 and Fig. 26 are compared, it is seen that, for the same momentary times, the less $L(t)/L(t=\infty)$ and $\Gamma(t)/\ (t=\infty)$ values have been obtained for NACA0012. Remember that this data is normalized, which shows that after a sudden jump in the

values, flat plate parameters fall down to 65% of the steady state values. Whereas, NACA0012 parameters fall down to 40%, which results in longer transient times for the airfoil. For this reason, parameters of the NACA0012 is slightly lower than the flat plate for the same momentary times.

Besides, when the Fig. 24 and Fig. 27 are compared, a change of the drag coefficient characteristic is also observed. At the very first moments of the motion, increasing drag force has been created on the body. Since the starting vortex creates negative drag force and it has more dominant effect on the body at the very first moments, for a starting vortex which has the larger amount of circulation leads to the visible dramatic change on the c_d curve. For this reason, there is a small hump in the c_d curve of NACA0012, whereas the curve of flat plate is monotonically decreasing. On the other hand, there is no considerable difference between the wake patterns.

4.2.2. Heaving Motion

The heaving motion analyses were done for the NACA0015 airfoil profile in three different cases and these analyses were validated by the experimental study by Bratt (Bratt (1953)). The first analysis was conducted for the $U_\infty/c=1.56\ s^{-1}$, $h_0/c=0.019$, $k=8.58$ and $U_\infty\Delta t/c=0.009$. Secondly, the analyses were conducted for the parameters $U_\infty/c=6.24\ s^{-1}$, $h_0/c=0.019$, $k=2.15$ and $U_\infty\Delta t/c=0.00225$. Finally, the parameters were assigned as $U_\infty/c=21.3\ s^{-1}$, $h_0/c=0.019$, $k=0.65$ and $U_\infty\Delta t/c=0.00065$. To obtain the specific patterns of the wake for each analysis, different travelling time values were preferred. Accordingly, the analyses were run for different number of iterations which are 150, 800, 3000 respectively; for each case, the variations of the normal, drag and moment coefficients w.r.t. time were plotted along its travelling time.

The variations of the normal coefficient which becomes the lift coefficient for the heaving motion, drag and the moment coefficients w.r.t. time, which were given in the Fig. 29, 30 and 31, for the first analysis. When the graphs for these coefficients are checked, at the very first moments (*until around the 0.04 s*), a transient behavior is observed. Except a small glitch at around $t=0.2$, the dynamics are almost periodically steady.

The normal, drag and moment coefficients regarding to the second analysis (faster freestream) were presented in the Fig. 34, 35 and 36. Since the analysis time step is much

shorter, the length of the analysis is just around one period. It is seen that as the freestream is increased the magnitudes of the all coefficients have reduced.

In the third analysis (the fastest freestream), since the given time step is considerably shorter, computation time is much longer relative to the other cases. Hence, the analysis for the normal, drag and moment coefficient has been able to run for a short time where only the beginning of the transient behavior can be observed. These plots were presented in the Fig. 39, 40 and 41. It is seen from all these figures that the coefficients have gotten even smaller. Therefore, it can be concluded that, as the freestream gets faster, the coefficients tend to get smaller.

Moreover, the wake pattern behind the airfoil which were calculated by the current method were presented in the Fig. 32, 37 and 42. In addition, the photos by experimental literature were shared in the Fig. 33, 38 and 43. When the photograph of the wake pattern in the Fig. 33 is checked, the mushroom shaped pattern which were obtained by the first analysis is the correct reflection of the wake shape. The comparison of the numerical and experimental patterns which were given in the Fig. 37 and 38 respectively also shows a well agreement. Furthermore, it can be expressed that, the slight curvature of the wake pattern in the third case was represented by the numerical model. Finally, it can be concluded that the wake analysis of the numerical is quite useful for the heaving motion of the NACA0015 airfoil.

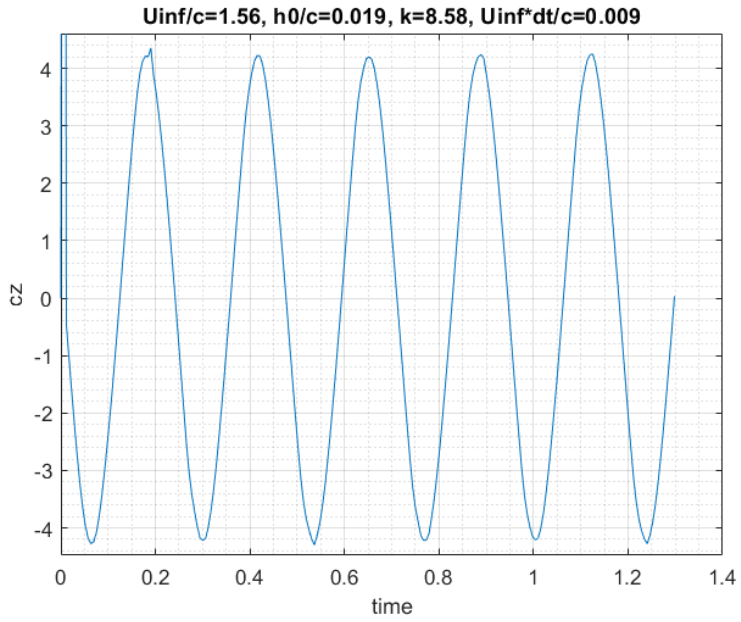

Figure 29. The normal coefficient variation of the NACA0015 w.r.t time: *$U_\infty/c=1.56\ s^{-1}$, $h_0/c=0.019$, $k=8.58$ and $U_\infty\Delta t/c=0.009$*

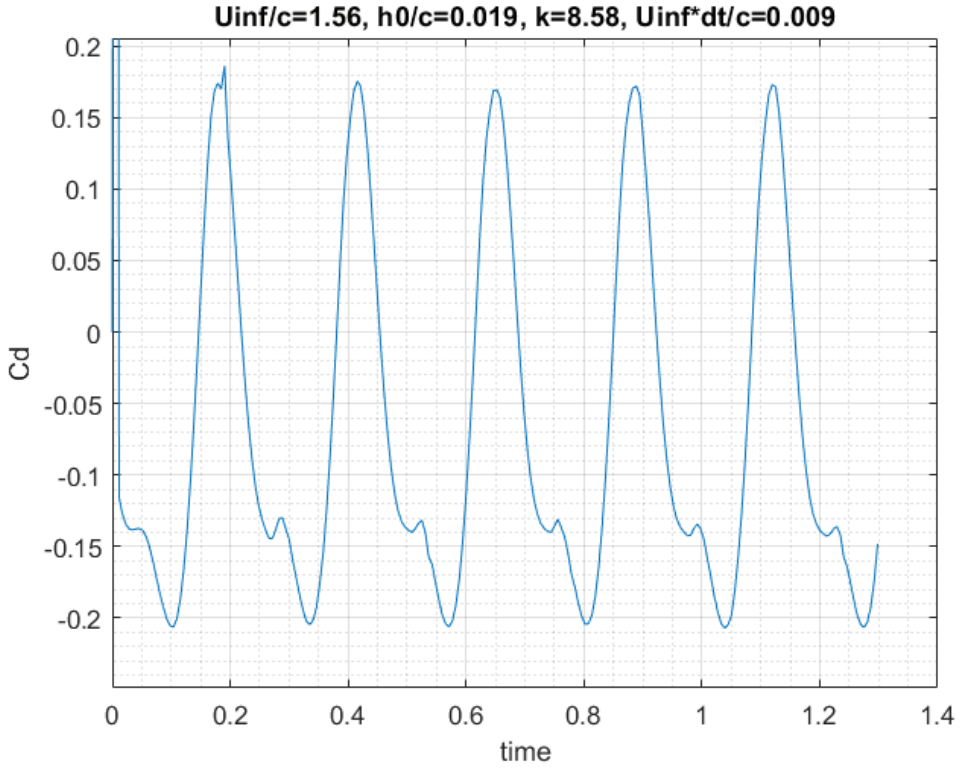

Figure 30. The drag coefficient variation of the NACA0015 w.r.t time: *$U_\infty/c=1.56\ s^{-1}$, $h_0/c=0.019$, $k=8.58$ and $U_\infty\Delta t/c=0.009$*

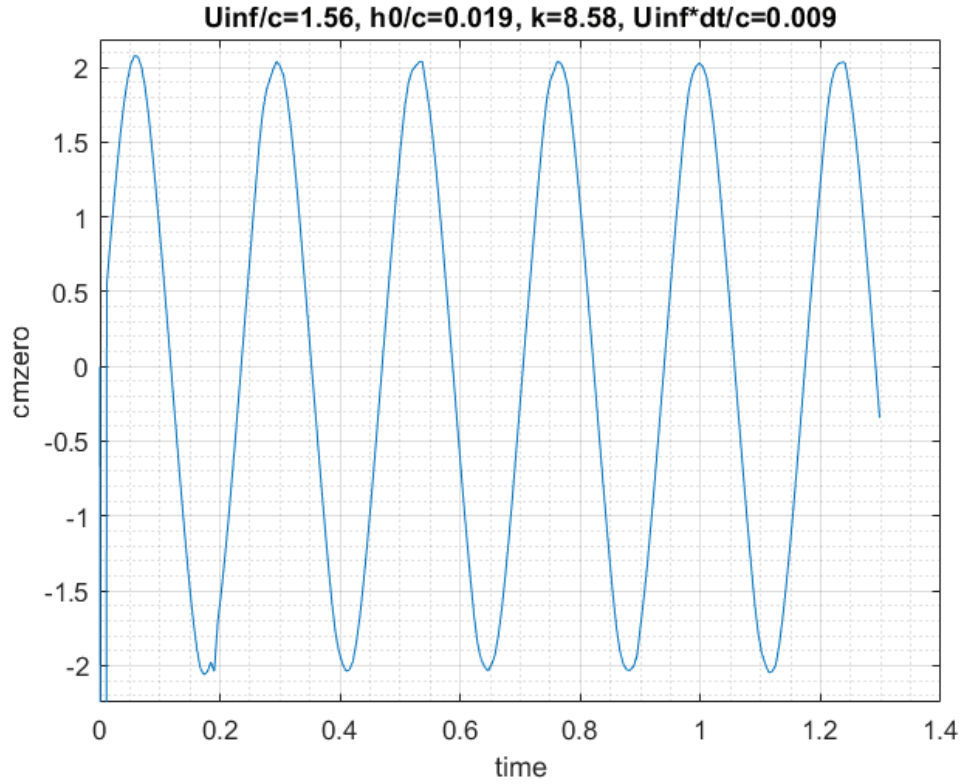

Figure 31. The moment coefficient variation of the NACA0015 w.r.t time: *$U_\infty/c=1.56\ s^{-1}$, $h_0/c=0.019$, $k=8.58$ and $U_\infty\Delta t/c=0.009$*

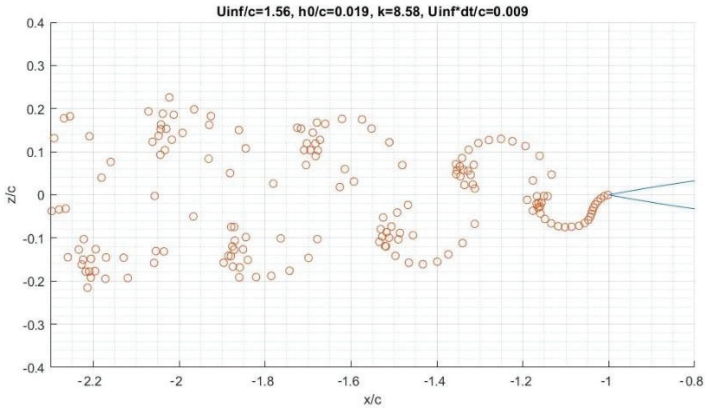

Figure 32. The analysis of the wake pattern of the NACA0015 in heaving motion: *$U_\infty/c=1.56\ s^{-1}$, $h_0/c=0.019$, $k=8.58$ and $U_\infty\Delta t/c=0.009$*

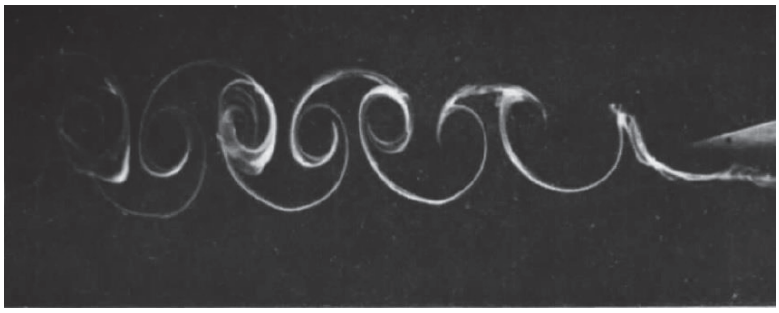

Figure 33. The visualization of the wake pattern of the NACA0015 in heaving motion by smoke trace: *$U_\infty/c=1.56\ s^{-1}$, $h_0/c=0.019$ and $k=8.58$*
(Source: Bratt (1953))

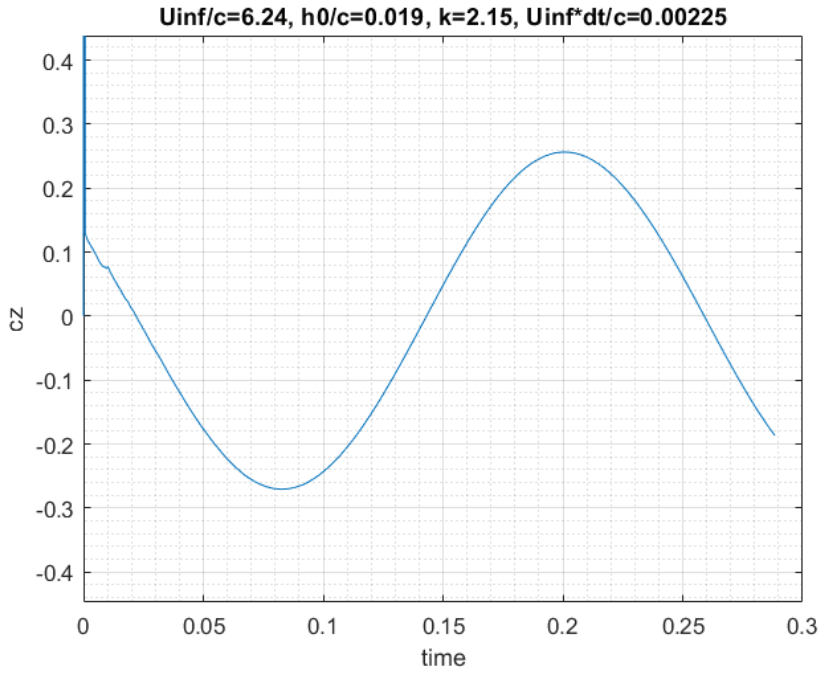

Figure 34. The normal coefficient variation of the NACA0015 w.r.t time: *$U_\infty/c=6.24\ s^{-1}$, $h_0/c=0.019$, $k=2.15$ and $U_\infty\Delta t/c=0.00225$*

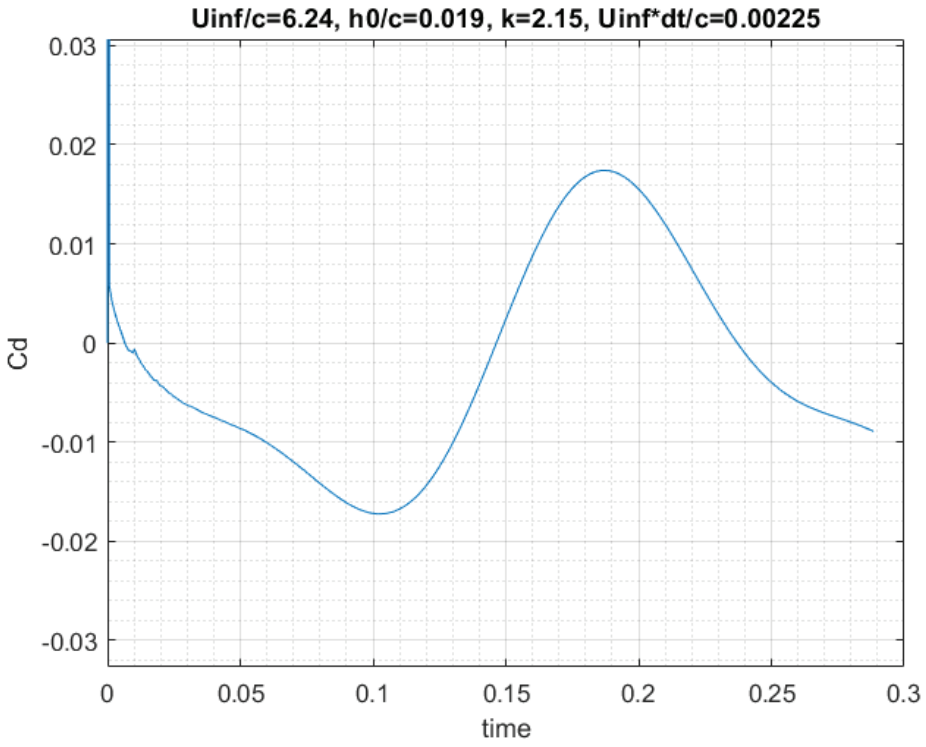

Figure 35. The drag coefficient variation of the NACA0015 w.r.t time:
$U_\infty/c=6.24\ s^{-1}$, $h_0/c=0.019$, $k=2.15$ and $U_\infty\Delta t/c=0.00225$

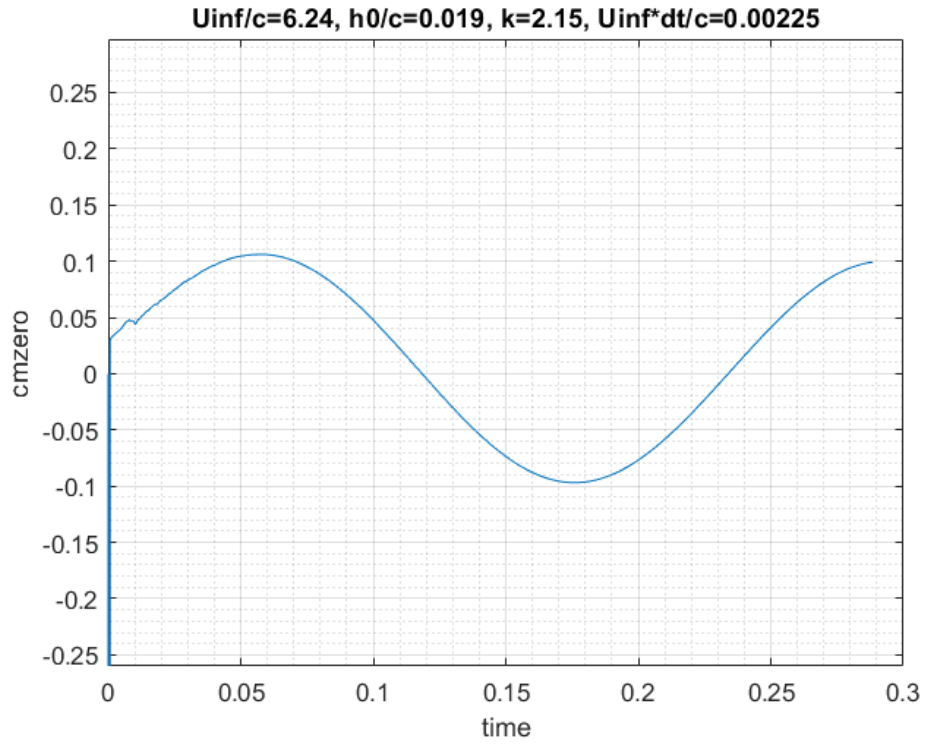

Figure 36. The moment coefficient variation of the NACA0015 w.r.t time:
$U_\infty/c=6.24\ s^{-1}$, $h_0/c=0.019$, $k=2.15$ and $U_\infty\Delta t/c=0.00225$

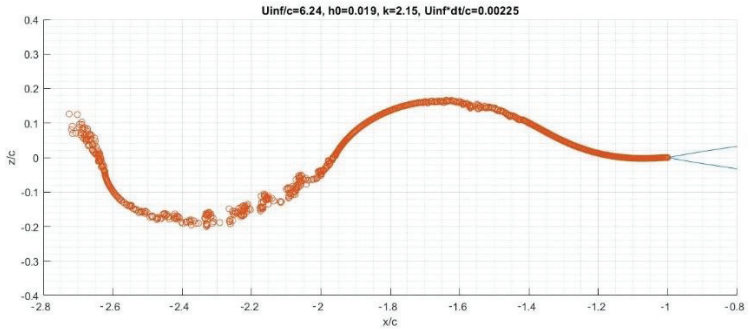

Figure 37. The analysis of the wake pattern of the NACA0015 in heaving motion: $U_\infty/c=6.24\ s^{-1}$, $h_0/c=0.019$, $k=2.15$ and $U_\infty\Delta t/c=0.00225$

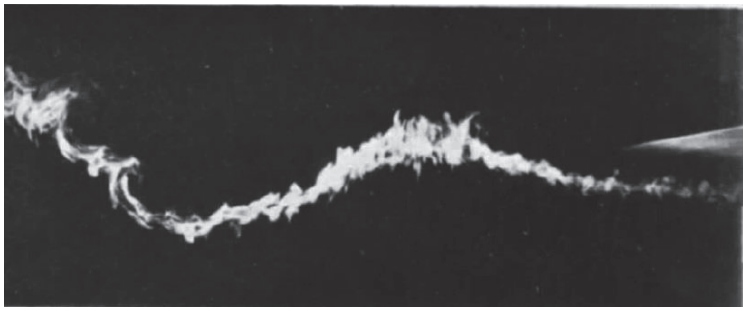

Figure 38. The visualization of the wake pattern of the NACA0015 in heaving motion by smoke trace: $U_\infty/c=6.24\ s^{-1}$, $h_0/c=0.019$ and $k=2.15$ (Source: Bratt (1953))

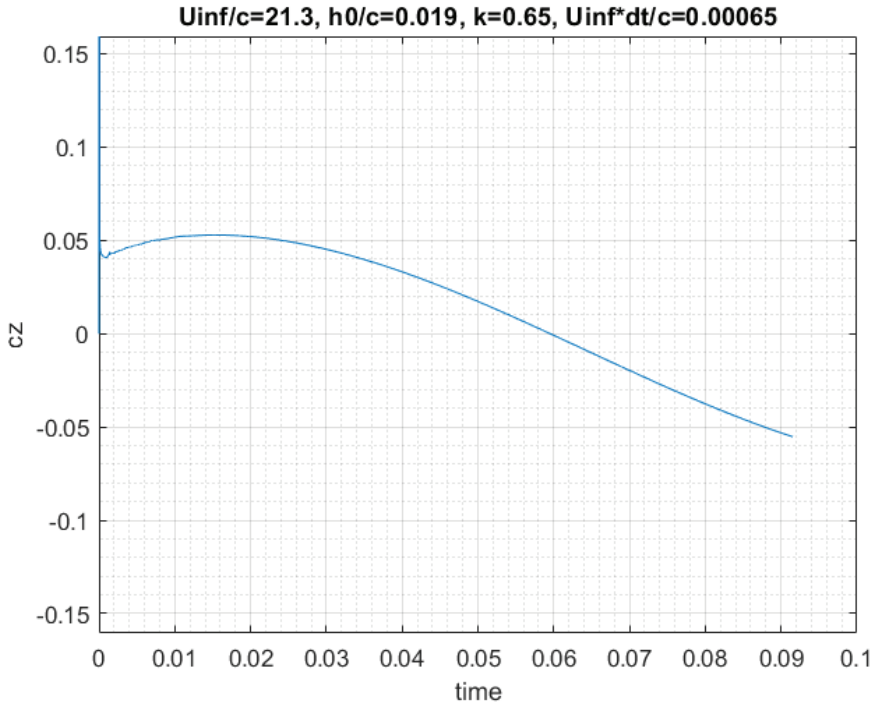

Figure 39. The normal coefficient variation of the NACA0015 w.r.t time: $U_\infty/c=21.3\ s^{-1}$, $h_0/c=0.019$, $k=0.65$ and $U_\infty\Delta t/c=0.00065$.

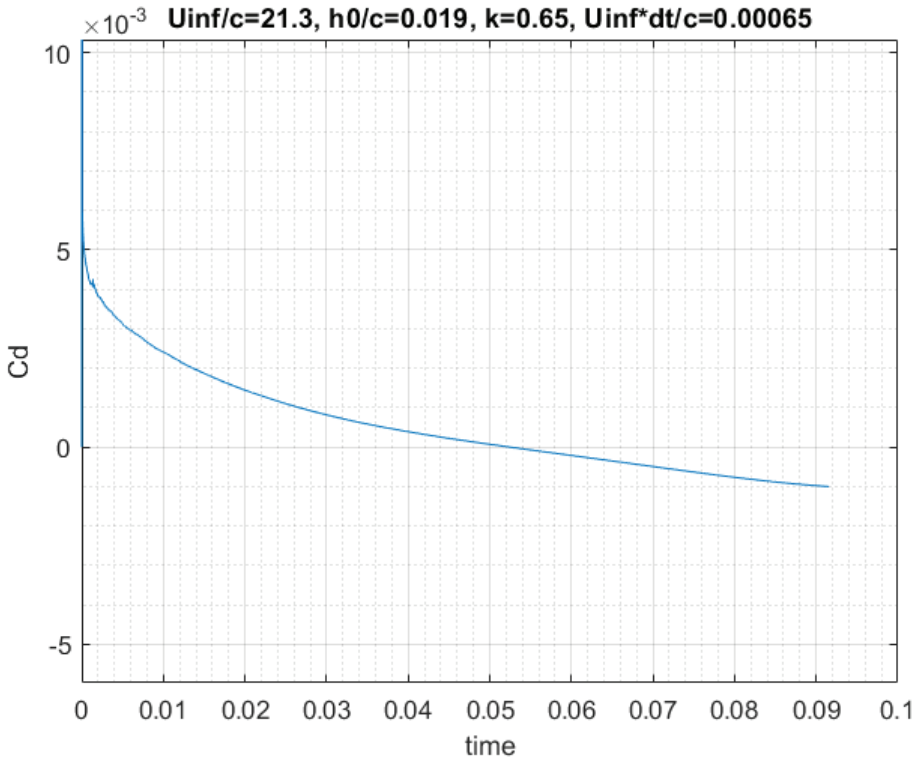

Figure 40. The drag coefficient variation of the NACA0015 w.r.t time: *$U_\infty/c=21.3\ s^{-1}$, $h_0/c=0.019$, $k=0.65$ and $U_\infty\Delta t/c=0.00065$.*

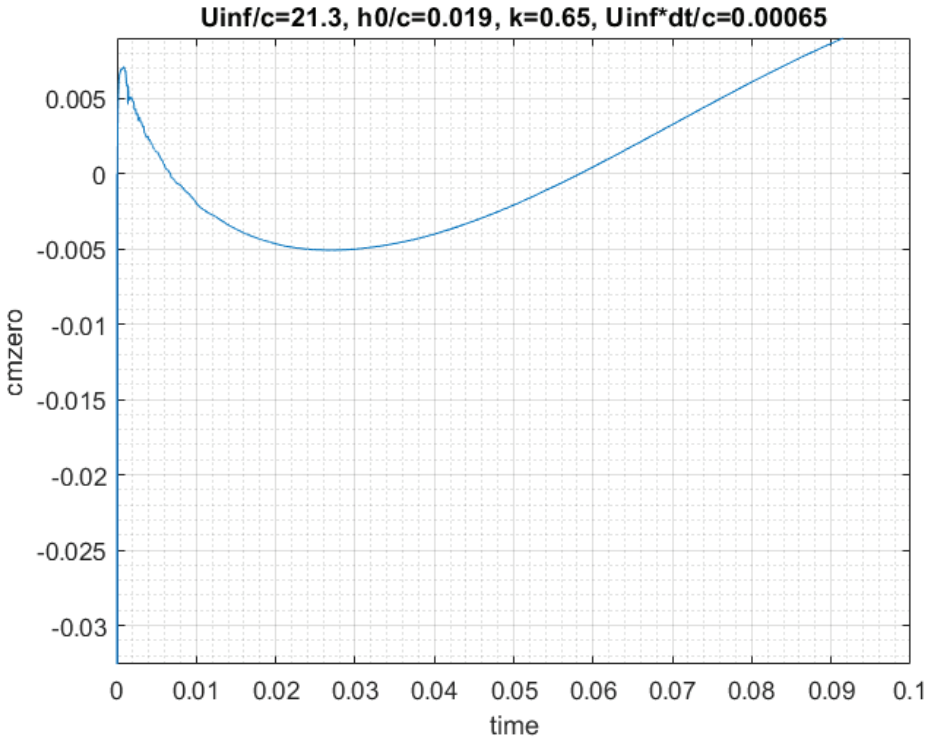

Figure 41. The moment coefficient variation of the NACA0015 w.r.t time: *$U_\infty/c=21.3\ s^{-1}$, $h_0/c=0.019$, $k=0.65$ and $U_\infty\Delta t/c=0.00065$.*

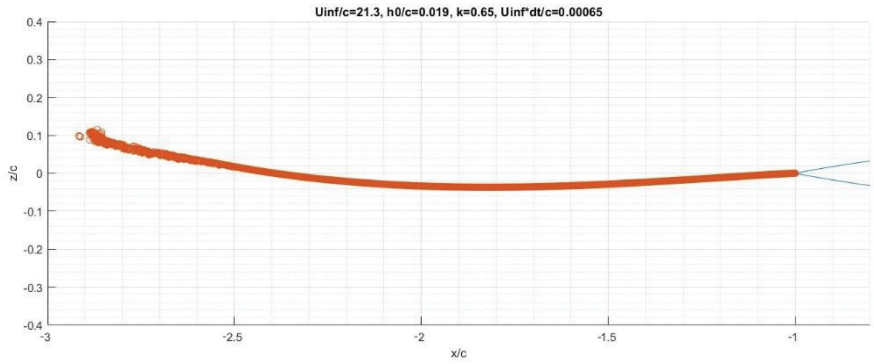

Figure 42. The analysis of the wake pattern of the NACA0015 in heaving motion: $U_\infty/c=21.3\ s^{-1}$, $h_0/c=0.019$, $k=0.65$ and $U_\infty\Delta t/c=0.00065$

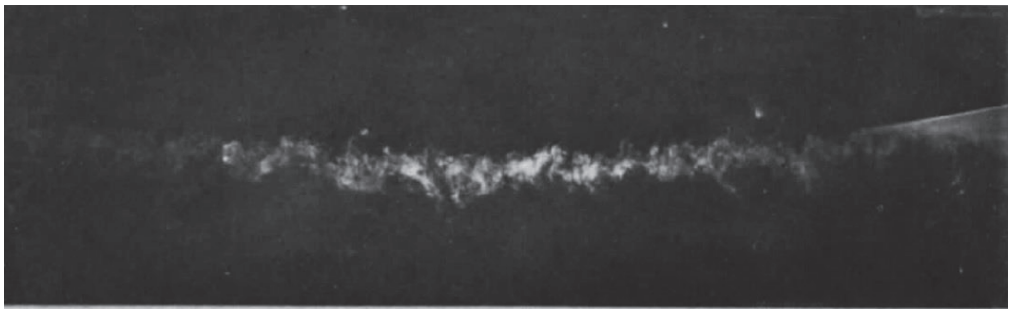

Figure 43. The visualization of the wake pattern of the NACA0015 in heaving motion by smoke trace: $U_\infty/c=21.3\ s^{-1}$, $h_0/c=0.019$ and $k=0.65$ (Source: Bratt (1953))

4.2.3. Pitching Motion

The pitching motion analyses were made for NACA0012 and NACA0015 airfoil profiles and the results were validated by the available experimental data in the literature. The simulations of NACA0012 were run for two different conditions. The first one is run for the conditions $\theta_m=4^o$, $\theta_a=6^o$, $l_{pa}=0.35$ and $k=0.021$ at $Re=1.63e6$. Secondly, the parameters were assigned as $\theta_m=3^o$, $\theta_a=10^o$, $l_{pa}=0.25$ and $k=0.1$ at $Q_\infty\Delta t/c=1$. The wake shape analyses were done for the conditions of $\theta_m=0^o$, $\theta_a=4^o$, $l_{pa}=0.25$, $k=8.96$.

The results of the first analysis of the lift coefficient for the NACA0012 are in the Fig. 44 and 45 respectively. The Fig. 45 includes the experimental data which were from the two different source (Sandia and Krzysiak) and the analysis of a numerical model which was a viscous-inviscid coupling technique of García (García (2011)). In this figure, *S* and *U* letters indicate the *steady* and *unsteady*. Since the loops of c_l w.r.t. α which has been given in the figures are compared, it can be deduced that, the analysis of the current method has similar results with the numerical method of the Garcia. When it is considered

that the current model did not include the viscous effects, it can be said that a kind of ability of this analysis is a success of the method. Moreover, since the experimental data of the drag and moment coefficients for the chosen parameters are not available, the comparison for the drag and moment characteristics of the current model and the model which was developed by the Garcia were made. The results were presented in the Fig. 46 and 47 respectively. The characteristics by the two numerical solutions are clearly different than each other. In here, it should be remembered that the model of the author includes the viscosity which plays a main role in the estimation of drag.

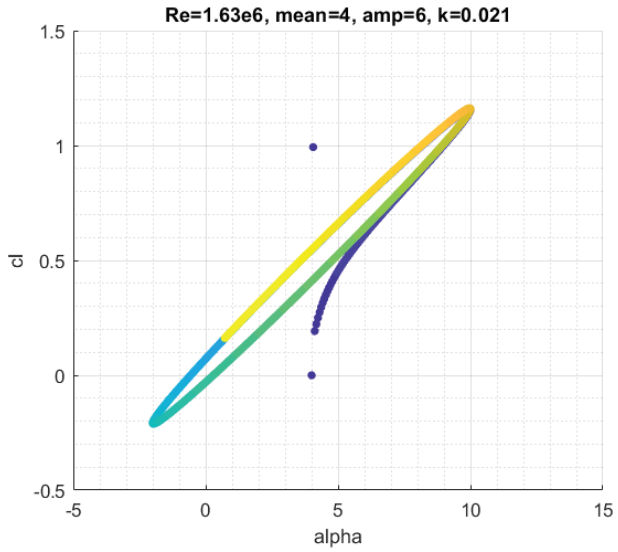

Figure 44. The numerical analysis of the lift coefficient variation for the NACA0012: w.r.t angle of attack: $\theta_m=4^o$, $\theta_a=6^o$, $l_{pa}=0.35$ and $k=0.021$ at $Re=1.63e6$.

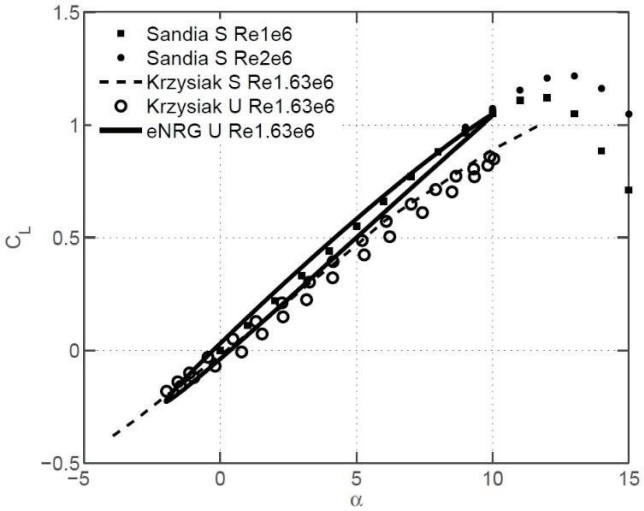

Figure 45. The literature data of the lift coefficient variation for the NACA0012 w.r.t angle of attack: $\theta_m=4^o$, $\theta_a=6^o$, $l_{pa}=0.35$ and $k=0.021$ at $Re=1.63e6$. (Source: García (2011))

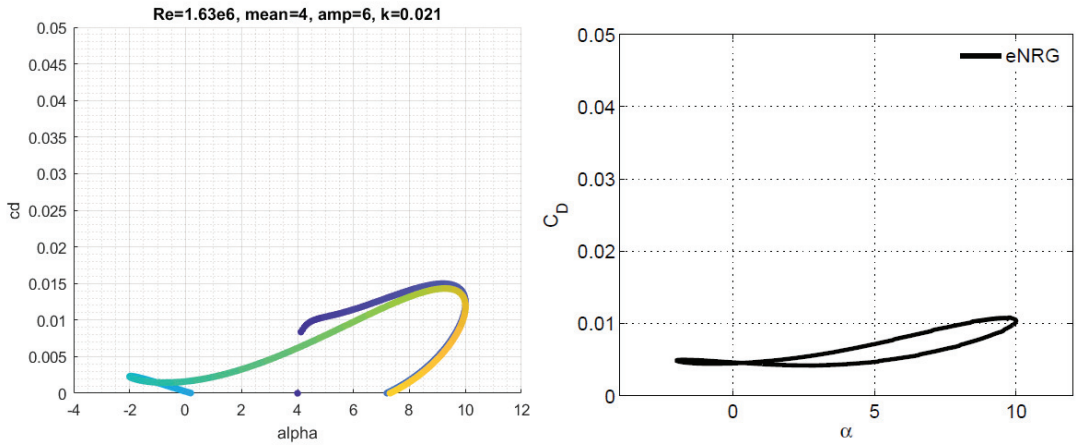

Figure 46. The comparison of the current method(left) and the literature data of the drag coefficient variation for the NACA0012 w.r.t. angle of attack: $\theta_m=4^o$, $\theta_a=6^o$, $l_{pa}=0.35$ and $k=0.021$ at $Re=1.63e6$. (Source: García (2011))

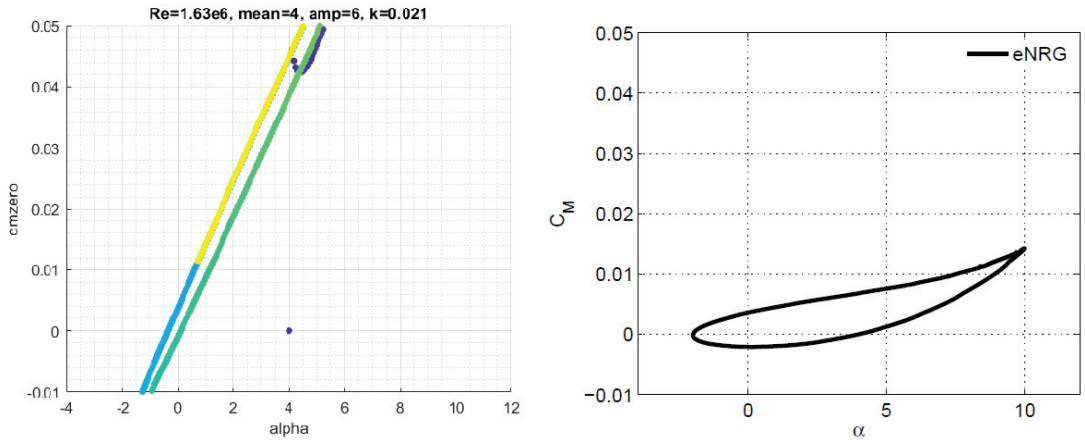

Figure 47. The comparison of the current method(left) and the literature data of moment coefficient variation for the NACA0012 w.r.t. angle of attack: $\theta_m=4^o$, $\theta_a=6^o$, $l_{pa}=0.35$ and $k=0.021$ at $Re=1.63e6$. (Source: García (2011))

The lift and moment characteristics of the second set of parameters which were obtained by the current model and the numerical model in the literature which was developed by the Katz and Maskew (Joseph Katz and MASKEW (1988)) for the NACA0012 were presented in the Fig. 48 and Fig. 49 respectively. In Fig. 43, the experimental data is represented by the dashed line. When the experimental data shown by the dashed lines are checked, it is seen that the model which was created by the authors is more advanced model in terms of the reflecting the curves.

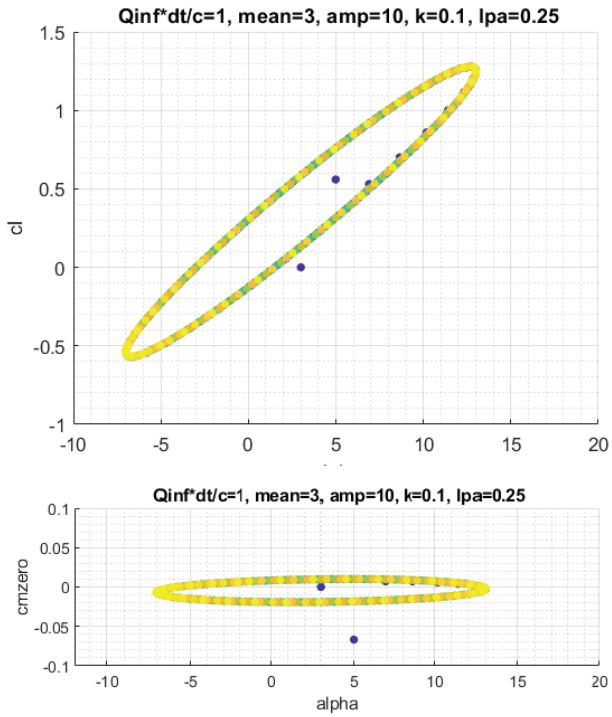

Figure 48. The lift and moment coefficient variations for the NACA0012 w.r.t. angle of attack: $\theta_m=3^o$, $\theta_a=10^o$, $l_{pa}=0.25$ and $k=0.1$ at $Q_\infty \Delta t/c=1$.

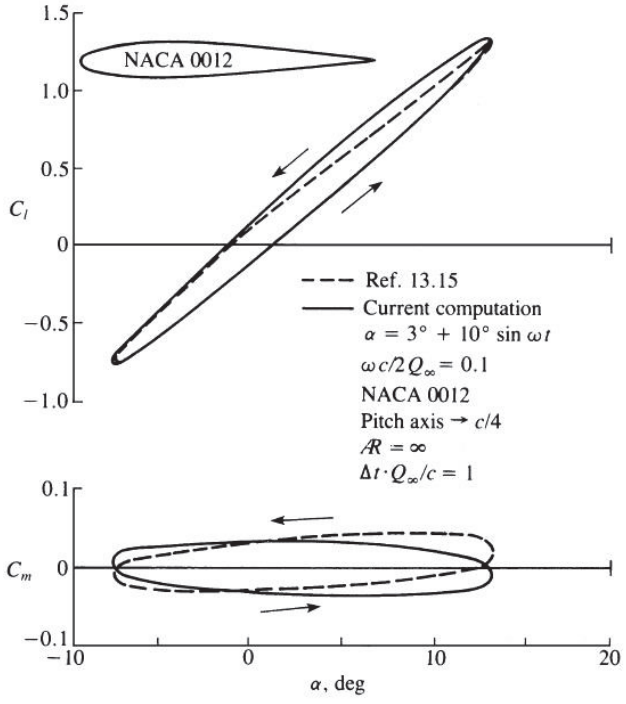

Figure 49. The lift and moment coefficient variations for the NACA0012 w.r.t. angle of attack: $\theta_m=3^o$, $\theta_a=10^o$, $l_{pa}=0.25$ and $k=0.1$ at $Q_\infty \Delta t/c=1$.
(The dashed lines are the experimental values)
(Source: Joseph Katz and MASKEW (1988))

Since, their model is a 3D model and has ability to include the effects of the flow separation; hence, their results are more realistic in these conditions. Nevertheless, for such the challenging conditions which includes the large pitching amplitude, the current model can be considered as useful in terms of the reflecting the range of lift and moment coefficients w.r.t. angle of attack even without including the flow separation.

The wake pattern estimation by the current model and experimental literature (Koochesfahani (1989)) were presented in the Fig. 50 and 51. According to the results it can be expressed that near the trailing edge of the airfoil, the created wake pattern was well estimated by the numerical model.

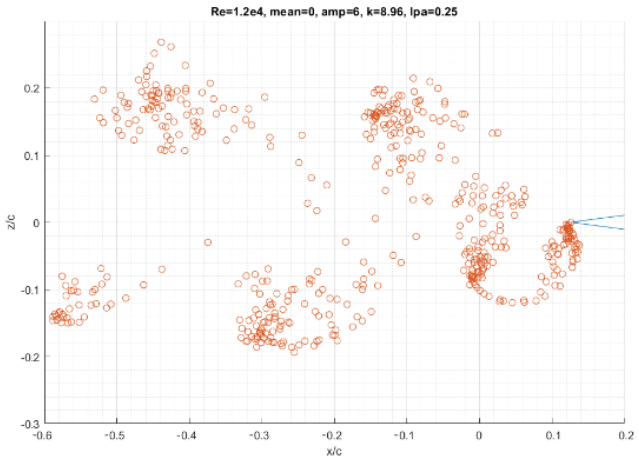

Figure 50. The wake pattern estimation for the NACA0012 in pitching motion: $\theta_m=0^o$, $\theta_a=4^o$, $l_{pa}=0.25$ and $k=8.96$ at $Re=1.2e4$.

Figure 51. The visualization of the wake pattern of the NACA0012 in pitching motion by dye: $\theta_m=0^o$, $\theta_a=4^o$, $l_{pa}=0.25$ and $k=8.96$ at $Re=1.2e4$.
(Source: Koochesfahani (1989))

CHAPTER 5

CONCLUSION

The flow around the airfoil profiles were obtained by using the potential flow based numerical panel methods. The two different models which were for the steady state and unsteady conditions were developed. For both the steady and unsteady models, the planar vortex panels were used to model the body. In addition, the point vortex was also used for the wake of the unsteady model. Steady state analyses were conducted for the lift coefficient of four different types of the airfoil. For the unsteady part, the dynamics of sudden forward, heaving and the pitching motions were investigated for different geometries and the set of parameters. The analyses for the lift, drag, moment coefficients, and wake patterns were carried out. The obtained results by the steady and unsteady models were compared with the available numerical and the experimental literature. Accordingly, followings are concluded:

- Steady state analysis for the pressure coefficient of NACA0012 at the angle of attack of $\alpha=9^{o}$ exactly matched with the same order of vortex panel model in the literature.
- The lift analyses for the NACA0012, 2412, 2418 and 4412 profiles by the current method showed a well agreement with the inviscid mode of the Xfoil. Besides, except the 4412 profile, the closer values than the Xfoil inviscid mode to the experimental data were attained.
- The sudden forward motion of a flat plate at the angle of attack of $\alpha=5^{o}$ was analyzed through the unsteady model. For the $Q_{\infty}\Delta t/c$=0.25, the current model derived the closer values to the Wagner's exact solution than the lumped vortex method trends for the lift, circulation and drag were successfully achieved.

- The heaving motion of NACA0015 analyses were done for the three different cases. The parameters of the first case are $U_\infty/c=1.56\ s^{-1}$, $h_0/c=0.019$, $k=8.58$ and $U_\infty\Delta t/c=0.009$. Secondly, the analyses were conducted for the parameters $U_\infty/c=6.24\ s^{-1}$, $h_0/c=0.019$, $k=2.15$ and $U_\infty\Delta t/c=0.00225$. Finally, the parameters were assigned as $U_\infty/c=21.3\ s^{-1}$, $h_0/c=0.019$, $k=0.65$ and $U_\infty\Delta t/c=0.00065$. The wake patterns behind the airfoil for these three cases which were also experimentally obtained were well captured. Moreover, the sinusoidal trends of the lift, drag and moment coefficients were achieved.
- The pitching motion of the NACA0012 was examined for the lift, drag and moment characteristics in two different case. The first set of parameters are $\theta_m=4^o$, $\theta_a=6^o$, $l_{pa}=0.35$ and $k=0.021$ at $Re=1.63e6$. For this case, since the model did not include the viscous effects the prediction of the lift loop of the pitching motion was limited. However, the lift characteristic results of the current method were very similar to the analysis by the Garcia's viscous-inviscid coupling model, which is a success for the current model. Secondly, the parameters were assigned as $\theta_m=3^o$, $\theta_a=10^o$, $l_{pa}=0.25$ and $k=0.1$ at $Q_\infty\Delta t/c=1$. It can be stated that, for this case the general trend was estimated fairly good. Lastly, for the given parameters of $\theta_m=0^o$, $\theta_a=4^o$, $l_{pa}=0.25$ and $k=8.96$ at $Re=1.2e4$ the wake pattern estimated by the current model and observed by the Koochesfahani were compared; the results are optimistic.

On the whole, it can be expressed that, since the viscous effects, flow separation etc. were not included, the current two models are limited in terms of the prediction of the pressure, lift, drag and moment coefficients. They can be mainly useful for the shrinking of the design domain. On the other hand, for the prediction of the wake patterns behind the body, the current unsteady model is quite advantageous. If the importance of the wake shape estimation in the wind turbine aerodynamics is considered, the model can be expressed as a useful tool even for its simple approach.

Besides, if these potential flow based numerical models are improved by including the viscosity, flow separation etc., their applicability will be increased to modelling wind turbine blade unsteady aerodynamics and therefore, performance characteristics can be obtained more realistically.

REFERENCES

Abbott, I. H., & Von Doenhoff, A. E. (1959). *Theory of wing sections, including a summary of airfoil data*: Courier Corporation.

Abbott, I. H., Von Doenhoff, A. E., & Stivers Jr, L. (1945). Summary of airfoil data.

Anderson, J. D. (2016). *Fundamentals of Aerodynamics*: McGraw-Hill Education.

Bratt, J. (1953). *Flow patterns in the wake of an oscillating aerofoil*: HM Stationery Office UK.

Drela, M. (2001). Xfoil (Version 6.9). http://web.mit.edu/drela/Public/web/xfoil/: Mark Drela, MIT Aero & Astro Harold Youngren, Aerocraft, Inc.

García, N. R. (2011). *Unsteady viscous-inviscid interaction technique for wind turbine airfoils.* Ph. D. Thesis, Technical University of Denmark, Lyngby, Denmark,

Katz, J., & MASKEW, R. (1988). Unsteady low-speed aerodynamic model for complete aircraft configurations. *Journal of Aircraft, 25*(4), 302-310.

Katz, J., & Plotkin, A. (1991). *Low-speed Aerodynamics: From Wing Theory to Panel Methods*: McGraw-Hill.

Katz, J., & Plotkin, A. (2001). *Low-speed aerodynamics* (Vol. 13): Cambridge university press.

Koochesfahani, M. M. (1989). Vortical patterns in the wake of an oscillating airfoil. *AIAA journal, 27*(9), 1200-1205.

Kuethe, A. M., & Chow, C. Y. (1997). *Foundations of Aerodynamics: Bases of Aerodynamic Design*: Wiley.

Pozrikidis, C. (2016). *Fluid dynamics: theory, computation, and numerical simulation*: Springer.

Tavoularis, S. (n.d.). THE VORTEX PANEL METHOD. Retrieved from http://by.genie.uottawa.ca/~mcg4345/AdditionalNotes/PanelMethod.pdf

Wagner, H. (1925). Über die Entstehung des dynamischen Auftriebes von Tragflügeln. *ZAMM-Journal of Applied Mathematics and Mechanics/Zeitschrift für Angewandte Mathematik und Mechanik, 5*(1), 17-35.

Zanon, A., Giannattasio, P., & Simão Ferreira, C. J. (2013). A vortex panel model for the simulation of the wake flow past a vertical axis wind turbine in dynamic stall. *Wind Energy, 16*(5), 661-680.